Magnetic detection and characterization of biogenic magnetic minerals: A comparison of ferromagnetic resonance and first-order reversal curve diagrams

Liao Chang[1,2], Andrew P. Roberts[2], Michael Winklhofer[3], David Heslop[2], Mark J. Dekkers[1], Wout Krijgsman[1], John D. Fitz Gerald[2], and Paul Smith[4]

[1]Paleomagnetic Laboratory "Fort Hoofddijk," Department of Earth Sciences, Utrecht University, Utrecht, Netherlands, [2]Research School of Earth Sciences, Australian National University, Canberra, ACT, Australia, [3]Department of Earth and Environmental Sciences, Ludwig-Maximilians-University Munich, Munich, Germany, [4]Research School of Chemistry, Australian National University, Canberra, ACT, Australia

Abstract Biogenic magnetic minerals produced by magnetotactic bacteria occur ubiquitously in natural aquatic environments. Their identification and characterization are important for interpretation of paleomagnetic and environmental magnetic records. We compare two magnetic methods for their identification and characterization in a diverse set of sedimentary environments: ferromagnetic resonance (FMR) spectroscopy and first-order reversal curve (FORC) diagrams, constrained by transmission electron microscope observations. The advantages and limitations of each method are evaluated. FMR analysis provides a strong diagnostic indicator because of its ability to detect the strong shape anisotropy that arises from the biogenic chain architecture, but it can be obscured in mixed magnetic mineral assemblages. We develop a new FMR fitting approach that enables separation and characterization of biogenic components in natural samples. FMR spectral fitting on magnetofossil-bearing samples does not always reveal a strong signature of biogenic magnetite with <111>-aligned chains, in contrast to whole magnetotactic bacteria cells. This indicates that strictly <111>-aligned chains are not as common in magnetofossil assemblages, due to either chain collapse or different crystallographic axis orientations. FORC analysis provides an excellent tool for isolating the biogenic component as a "central ridge" signature with peak switching field distribution between ~20 and 60 mT. We also analyzed tuff samples with similar FMR characteristics to biogenic magnetite chains, which can cause ambiguity. We propose a magnetic protocol to improve the robustness and efficiency of biogenic magnetite identification and past microbial activity in a wide range of environments.

1. Introduction

Intracellular biomineralization of magnetite (Fe_3O_4) and greigite (Fe_3S_4) nanocrystals (magnetosomes) by magnetotactic bacteria (MTB) is a common biochemical process in natural environments. Magnetosomes are of great interest in biomagnetism and rock magnetism because of their distinct structural and magnetic properties, such as their precisely controlled size and morphology, single domain (SD) magnetic behavior, high purity and crystallinity, and hierarchical chain assembly [*Faivre and Schüler*, 2008]. Biogenic magnetic minerals occur frequently in modern environments [*Bazylinski and Frankel*, 2004] and their fossil remains (magnetofossils) have also been found globally within sediments and sedimentary rocks over geologically significant periods [e.g., *Kirschvink and Chang*, 1984; *Petersen et al.*, 1986; *Stoltz et al.*, 1986; *Vali et al.*, 1987; *Hounslow and Maher*, 1996; *Kopp et al.*, 2007, 2009; *Vasiliev et al.*, 2008; *Abrajevitch and Kodama*, 2009; *Roberts et al.*, 2011, 2012, 2013; *Larrasoaña et al.*, 2012; *Yamazaki and Ikehara*, 2012; *Heslop et al.*, 2013; *Reinholdsson et al.*, 2013]. Magnetofossils can make important contributions to paleomagnetic records because of their stable SD remanence, although a range of geological and environmental processes can decrease this stability by destroying the original chain configuration. Magnetofossils are also potentially important in paleoenvironmental studies because they can reflect past microbiological activity and geochemical conditions that controlled their growth and preservation [e.g., *Hesse*, 1994; *Lean and McCave*, 1998; *Kopp and Kirschvink*, 2008; *Roberts et al.*, 2011; *Chang et al.*, 2012a; *Larrasoaña et al.*, 2012; *Yamazaki and Ikehara*, 2012; *Reinholdsson et al.*, 2013].

It is relatively straightforward to detect living magnetotactic bacterial cells using light microscopy and a bar magnet due to motility of MTB with respect to an external magnetic field in aqueous environments.

Magnetofossils have distinctive crystal morphologies, narrow particle size distributions, and chain structures that can be observed directly with transmission electron microscope (TEM) imaging of magnetic mineral extracts from natural samples [e.g., *Petersen et al.*, 1986; *Stoltz et al.*, 1986; *Vali et al.*, 1987; *Peck and King*, 1996; *Lean and McCave*, 1998; *Hounslow and Maher*, 1996; *Roberts et al.*, 2011; *Chang et al.*, 2012a; *Larrasoaña et al.*, 2012; *Yamazaki and Ikehara*, 2012]. However, the magnetic extraction process can affect the original magnetofossil configuration by disrupting the chain structure. It is also difficult to image magnetosomes if their concentration is low and they have been consolidated in the sediment matrix. Most importantly, however, the time-consuming nature of TEM analysis precludes processing of large numbers of samples. In contrast, rock magnetic techniques have the advantages of being rapid to apply and mostly nondestructive for screening large sample sets to detect possible magnetofossil occurrences. These methods include low-temperature magnetism [e.g., *Moskowitz et al.*, 1993, 2008; *Carter-Stiglitz et al.*, 2004; *Weiss et al.*, 2004; *Chang et al.*, 2013], coercivity analysis of isothermal remanent magnetization (IRM) acquisition curves [e.g., *Kruiver and Passier*, 2001; *Egli*, 2004a, 2004b], ferromagnetic resonance (FMR) spectroscopy [*Weiss et al.*, 2004; *Kopp et al.*, 2006a, 2006b], and first-order reversal curve (FORC) diagrams [*Pike et al.*, 1999; *Roberts et al.*, 2000; *Egli et al.*, 2010]. Among these methods, FORC diagrams and FMR analyses at room temperature enable detection of the magnetosome chain structure and are less sensitive to surficial oxidation of magnetite, which can compromise low-temperature remanence warming tests [*Moskowitz et al.*, 1993, 2008; *Smirnov and Tarduno*, 2000; *Passier and Dekkers*, 2002; *Housen and Moskowitz*, 2006; *Roberts et al.*, 2012; *Chang et al.*, 2013]. In addition, low-temperature FMR analysis can provide sensitive detection of biogenic magnetite oxidation when samples are measured across the Verwey transition [*Gehring et al.*, 2012]. Combined FORC and FMR analysis has enabled identification of biogenic magnetite in carbonate-rich and other sediments [*Kopp et al.*, 2007; *Kind et al.*, 2011, 2012; *Roberts et al.*, 2011, 2012, 2013; *Larrasoaña et al.*, 2012; *Kodama et al.*, 2013]. In this study, we perform FMR and FORC analyses, assisted by TEM observations, on several types of sediments, including pelagic carbonates, continental margin marine sediments, lake sediments, and continental loess and paleosol deposits. In addition, we carried out FMR analysis on a range of natural samples from the Tiva Canyon (TC) tuff that lack magnetostatic interactions and possess a continuous evolution of narrowly distributed grain sizes [*Rosenbaum*, 1993; *Worm and Jackson*, 1999; *Roberts et al.*, 2000; *Pike et al.*, 2001a; *Jackson et al.*, 2006; *Till et al.*, 2011], in order to isolate the effects of magnetostatic interactions and magnetic anisotropy on FMR spectra. We test the suggestion that the unique properties of biogenic magnetic minerals produce a range of characteristic FMR signatures that are not known for other forms of natural samples [e.g., *Weiss et al.*, 2004; *Kopp et al.*, 2006a, 2006b]. In addition, we simulate a range of FMR spectra and develop a fitting approach to characterize biogenic minerals in magnetically mixed samples. FMR and FORC results are used to constrain interpretations about the presence and characteristics of biogenic magnetic minerals. The advantages and limitations of each method are discussed, and a protocol is suggested for optimizing magnetic detection of biogenic magnetic minerals.

2. Samples

We analyzed a range of samples (Figure 1), including pelagic marine sediments (samples "ODP689D-11R2-119" and "DSDP523-26H1-5"), continental margin marine sediments (samples "MD00-2361-XXX," "MD01-2421-XX-YY," and "CD143-55705-XX-YY"; where "XXX" indicates depth in centimeters, and "XX" and "YY" indicate core section number and depth interval, respectively), lake sediments ("BA-XXX" and "BG-XXX"), and continental deposits (Chinese loess/paleosols "YB-X-XX," and Czech paleosol "B-90"). Analyzing these diverse samples enables assessment of the usefulness of FMR and FORC measurements for detecting magnetofossils. Sample ODP689D-11R2-119 [*Florindo and Roberts*, 2005] is an Oligocene pelagic carbonate from Ocean Drilling Program (ODP) Site 689D, Maud Rise, Weddell Sea (64°31.01′S; 03°06.00–03°06.30′E; 2080 m water depth). Sample DSDP523-26H1-5 [*Bohaty et al.*, 2009] is a middle Eocene pelagic sediment collected from Deep Sea Drilling Project (DSDP) Site 523, South Atlantic Ocean (28°33.13′S, 02°15.08′W; 4572 m water depth).

Samples "MD00-2361-XX-XX" are Quaternary sediments from core MD00-2361 (113°28.63′E, 22°04.92′S), which was taken offshore of Western Australia (1805 m water depth) [*Heslop et al.*, 2013]. Samples "CD143-55705-XX-XX" are surface sediments from piston core CD143-55705 [*Rowan et al.*, 2009] on the Oman margin, northwestern Arabian Sea (22°22.4′N, 60°08.0′E; 2193 m water depth). Samples "MD01-2421-XX-XX" are Quaternary sediments collected from piston core MD01-2421 from the continental slope offshore of central Japan (36°01.4′N, 141°46.8′E; 2224 m water depth) [*Oba et al.*, 2006].
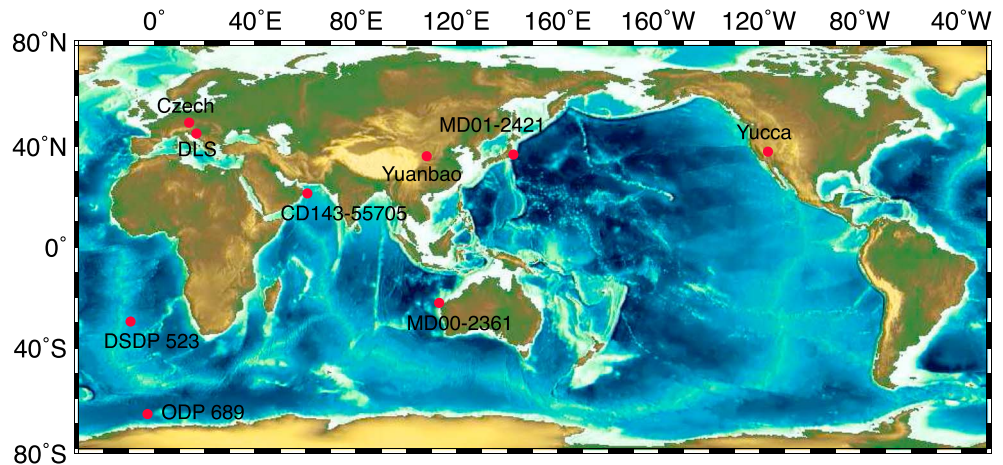
Figure 1. Map with locations from which results are presented for sedimentary samples in this study. See text for details of studied samples and locations.

Samples BA-XXX and BG-XXX are Miocene sediments from the ancient Dinaride Lake System (DLS) from Croatia, and Bosnia and Herzegovina. Samples BA-XXX are from outcrops in the open-pit coal mine of the Banović Basin [*de Leeuw et al.*, 2011]. Samples BG-XXX are from the Bugojno Basin in Bosnia and Herzegovina [*de Leeuw et al.*, 2012].

Samples YB-X-XX are weakly consolidated Holocene Chinese loess/paleosols from Yuanbao, western Chinese Loess Plateau [*Zhao and Roberts*, 2010]. B-90 is a Quaternary paleosol sample from south Moravia, southern Czech Republic [*van Oorschot et al.*, 2002]. We also analyzed inorganic samples to compare with magnetofossil-bearing samples. Samples labeled "TCXX" are from the Tiva Canyon (TC) ash flow tuff, Yucca Mountain, southern Nevada (36.82°N, 116.47°W) [e.g., *Schlinger et al.*, 1991; *Rosenbaum*, 1993; *Till et al.*, 2011]. TEM observations on samples from lower stratigraphic levels indicate an Fe oxide composition close to that of magnetite [*Schlinger et al.*, 1991]. With increasing stratigraphic level, there is a small increase in Ti content within magnetite, and also an increased average particle size. From the base to the top of the section, magnetic properties change continuously from dominantly superparamagnetic (SP) to SD [*Till et al.*, 2011]. Grain size distributions and magnetic properties of these samples were reported by *Schlinger et al.* [1991] and *Till et al.* [2011], respectively.

3. Methods

FMR spectroscopy measures absorption of microwave radiation by exchange-coupled magnetic systems as a function of the applied direct current (DC) field. FMR originates from magnetic field-induced precessional motion of magnetic moments. Resonance absorption occurs whenever the precession frequency is equal to the frequency v of the microwave magnetic field, which is applied perpendicular to the DC field B:

$$hv = g\mu_B B, \tag{1}$$

where $h = 6.626 \times 10^{-34}$ J s is Planck's constant, g is the spectroscopic splitting factor, and $\mu_B = 9.274 \times 10^{-24}$ J/T is the Bohr magneton. The effective g value of a sample is given by $g_{eff} = hv/\mu_B B_{eff}$, where B_{eff} is the effective magnetic field, which is the field at which maximum absorption occurs, or equivalently, the zero crossing field in the derivative absorption spectrum. B_{low}, B_{high}, ΔB_{FWHM}, and A are defined in the absorption spectra [e.g., *Weiss et al.*, 2004; *Kopp et al.*, 2006a, 2006b]. B_{low} and B_{high} are the magnetic fields where the absorption is half the maximum value at the low- and high-field ends of the peak, respectively. ΔB_{low} and ΔB_{high} are the low- and high-field linewidths, respectively. Their sum gives ΔB_{FWHM}. The asymmetry ratio A is defined as $A = \Delta B_{high}/\Delta B_{low}$. An empirical parameter that combines the FMR parameters A and ΔB_{FWHM} is denoted by α. It is defined as $\alpha = 0.17 A + 9.8 \times 10^{-4} \Delta B_{FWHM}$ [*Kopp et al.*, 2006a]. FMR spectra were measured with an X-band JEOL electron paramagnetic resonance (EPR) spectrometer at the Department of Chemistry of the Technical University of Munich, Germany, or with an X-band Bruker Elexys EPR spectrometer at the Research School of Chemistry and Research School of Earth Sciences,
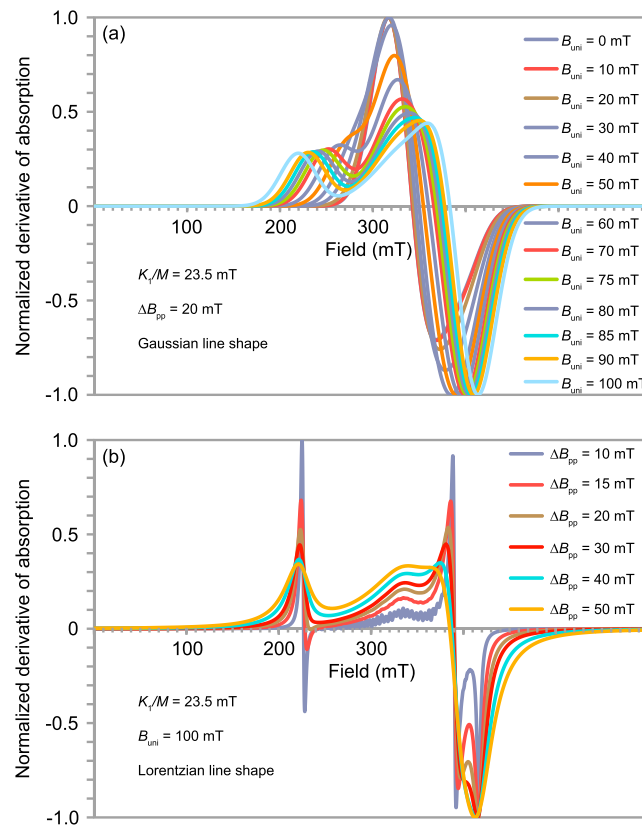
Figure 2. Simulation of FMR spectra for magnetite chains using the model of *Charilaou et al.* [2011a]: (a) evolution of simulated FMR spectra with increasing uniaxial anisotropy (B_{uni}) and (b) evolution of simulated FMR spectra with increasing Lorentzian line broading (ΔB_{pp}). In Figure 2a, a magnetocrystalline anisotropy $K_1/M_s = 23.5$ mT (where K_1 and M_s are the first magnetocrystalline anisotropy constant and saturation magnetization, respectively) and a Gaussian line broadening $\Delta B_{pp} = 20$ mT are used, while the uniaxial anisotropy field was varied from 0 to 100 mT. In Figure 2b, magnetocrystalline anisotropy $B_{cubic} = K_1/M_s = 23.5$ mT and a uniaxial anisotropy $B_{uni} = 100$ mT are used; the Lorentzian line broadening was varied between 10 and 50 mT.

Australian National University. For each measurement, 30–100 mg of air-dried sediment was microwaved at a frequency of 9.0–9.7 GHz and power of 0.6–2 mW.

Theoretical FMR spectra were simulated using the model of *Charilaou et al.* [2011a]. In this model, a single ellipsoid is employed to approximate a linear chain of magnetite crystals. The long axis of the ellipsoid lies along an easy axis <111> of the cubic magnetocrystalline anisotropy of magnetite. The modeled ellipsoid is treated as a Stoner-Wohlfarth SD particle, which is always homogeneously magnetized. Simulated spectra provide theoretical biogenic FMR components, with which to decompose experimental FMR spectra (Figure 2). In our new FMR decomposition procedure, in order to represent the contribution of magnetosomes to an FMR spectrum, we calculated over 3000 theoretical spectra, each with a uniaxial anisotropy in the 0–150 mT interval and a cubic anisotropy in the −30 to −20 mT interval. A given experimental spectrum was compared to each theoretical spectrum in an iterative manner. This involved optimizing the relative contribution of an individual theoretical spectrum based on the assumption that any resulting deviations from the experimental spectrum correspond to an isotropic component that can be approximated with the derivative of a Gaussian probability distribution function. After testing all theoretical spectra, the best fit combination of anisotropic and isotropic components was selected to represent the decomposed experimental spectrum.

Two approaches were proposed for decomposing FMR spectra for magnetofossil-bearing samples. One is based on approximate evaluation of the FMR condition to first order for either uniaxial or cubic anisotropy [*Kopp et al.*, 2006a, 2006b]. Sedimentary components modeled with this method have been interpreted as biogenic magnetite [*Maloof et al.*, 2007; *Kodama et al.*, 2013]. These model biogenic components, however, are not likely to represent true physical components because the cubic anisotropy of magnetite was neglected. The shortcomings of this approach are apparent from its application to analysis of MTB samples: for strain MV-1, model components have a g factor of 2.2 or greater [*Kopp et al.*, 2006b], which significantly exceeds the values for magnetite (2.12 [*Bickford*, 1950]) or maghemite (1.97 [*Valstyn et al.*, 1962]). Likewise, for relatively strong anisotropy field B_{an} relative to the applied DC field B_{app}, approximate evaluation of the resonance condition to first order in B_{an}/B_{app} yields a distorted FMR spectrum compared to that produced by exact evaluation of the resonance condition [*Winklhofer et al.*, 2014]. For MV-1, B_{an} was obtained as 170 mT [*Kopp et al.*, 2006b], which is not small compared to B_{app} under typical X-band magnetic fields of 300 mT.
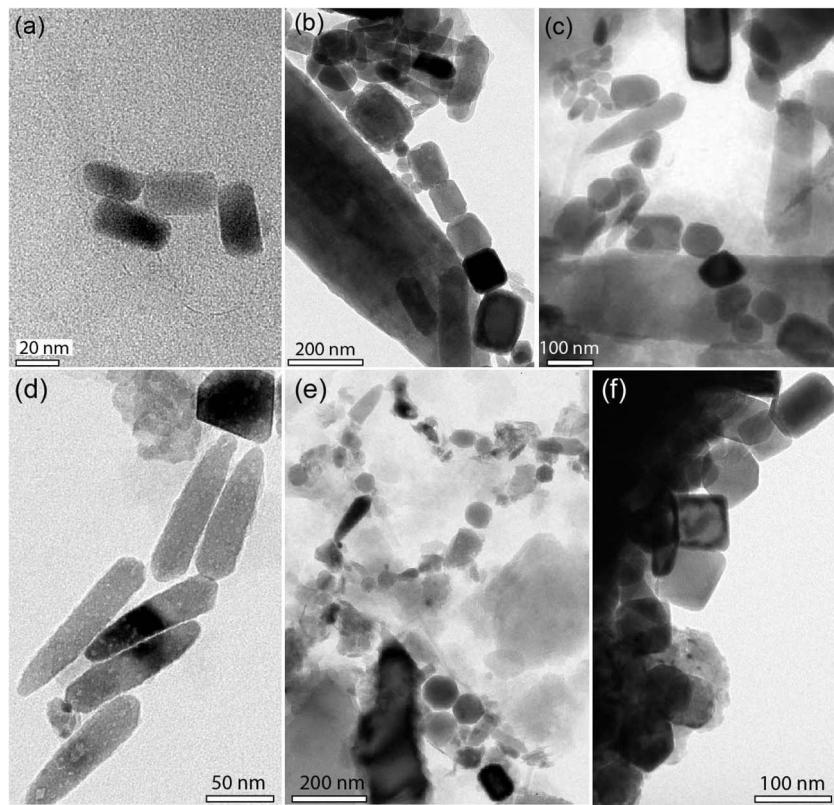
Figure 3. TEM images of magnetic mineral extracts of sedimentary samples from (a) ODP Hole 689D (at 122.11 mbsf), (b–e) core MD00-2361 offshore of Western Australia, and (f) core CD143-55705 from the Oman margin (at 21 cm). A glacial carbonate-rich sample (at 3.15 m) from core MD00-2361 (Figures 3b and 3c) and a clay-rich interglacial sample (at 1.25 m) from core MD00-2361 (Figures 3d and 3e). All samples contain abundant biogenic magnetite crystals.

In a second heuristic approach for FMR spectral decomposition [*Gehring et al.*, 2011], a quasi-isotropic FMR end-member component of adjustable linewidth and line shape is subtracted to isolate the anisotropic end-member in the remaining spectrum due to intact magnetosome chains. This approach relies on a correct guess of one end-member to obtain the other, which prompts the question whether extracted model components represent physical components. In our FMR fitting approach, we use the FMR model of *Charilaou et al.* [2011a], where the exact resonance condition is evaluated for a combined uniaxial and cubic anisotropy rather than using a first-order approximation, to generate more accurate biogenic magnetite components. A least squares approach is used to give the best fit to experimental FMR spectra.

FORC measurements were carried out with a Princeton Measurements Corporation MicroMag alternating gradient magnetometer (AGM Model 2900; noise level 2×10^{-9} A m^2) at the paleomagnetic laboratory of Utrecht University, Netherlands. FORC diagrams [*Pike et al.*, 1999; *Roberts et al.*, 2000] were obtained by measuring ~300–500 FORCs to maximum applied fields of 1 T, with averaging times of 150–250 ms. FORC diagrams were calculated using the "FORCme" software package of *Heslop and Roberts* [2012].

Magnetic separation was performed following the procedure of *Chang et al.* [2012a]. Magnetic extracts were imaged using a Philips CM300 TEM operated at 300 kV at the Research School of Earth Sciences, Australian National University. An EDAX Phoenix retractable X-ray detector and a Gatan 1024×1024 CCD camera were used.

4. Results

4.1. TEM Observations

TEM analysis was performed on selected samples, including pelagic carbonate from core ODP 689D at 122.11 meters below seafloor (mbsf) (Figure 3a), a carbonate-rich glacial sediment at 3.15 m (Figures 3b and 3c) and a clay-rich interglacial sediment at 1.25 m (Figures 3d and 3e) from core MD00-2361 offshore of Western Australia,
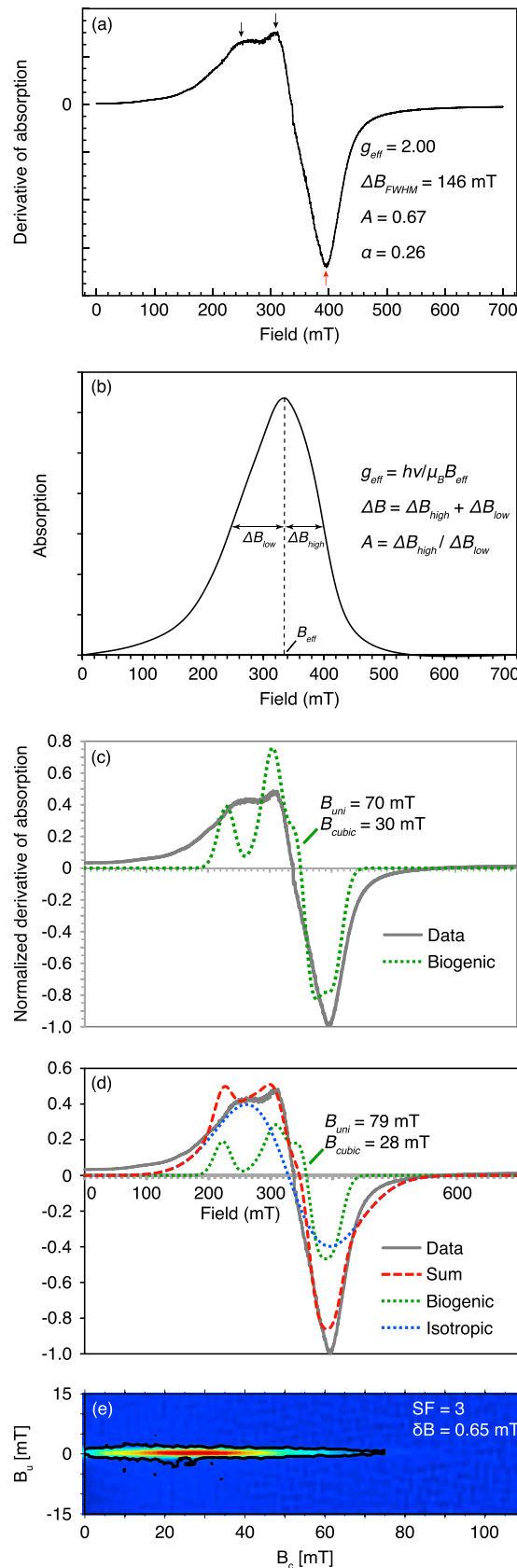
Figure 4

and surface sediment from a depth of 21 cm from core CD143-55705 (Figure 3f). TEM observations on these samples indicate abundant magnetite crystals. Their sizes fall within the region expected for biogenic magnetite. They also have a range of crystal morphologies, such as prisms, octahedra, and bullet shapes. All these properties are characteristic of magnetofossils [e.g., *Petersen et al.*, 1986; *Stoltz et al.*, 1986; *Vali et al.*, 1987; *Peck and King*, 1996; *Lean and McCave*, 1998; *Hounslow and Maher*, 1996; *Roberts et al.*, 2011; *Chang et al.*, 2012a; *Larrasoaña et al.*, 2012; *Yamazaki and Ikehara*, 2012]. These TEM observations provide direct confirmation of the presence of biogenic magnetite within the studied samples, which is crucial for the following interpretations of the FMR and FORC signatures of biogenic magnetite.

4.2. FMR and FORC Diagrams
4.2.1. Pelagic Marine Carbonate
We first present a characteristic FMR spectrum and FORC diagram for a pelagic marine carbonate (ODP689D-11R2-119; Figure 4) as an end-member for natural sedimentary samples in which biogenic magnetite dominates the magnetic mineral assemblages [*Roberts et al.*, 2012, 2013] to compare with results from other sediment types. Typical FMR derivative spectra for marine carbonates contain multiple low-field peaks (mostly two) and a pronounced high-field minimum (Figure 4a). FMR parameters fall within the region where $g_{eff} < 2.1$, $A < 1$, and $\alpha < 0.3$ (Table 1) [*Weiss et al.*, 2004; *Kopp et al.*, 2006a, 2006b]. FMR spectral fitting of this sample indicates that a single biogenic FMR component cannot fully explain the experimental spectrum (Figure 4c). An improved fit is provided by inclusion of a symmetrical isotropic component (Figure 4d). A FORC diagram for the pelagic carbonate has a dominant FORC distribution with negligible vertical spread (Figure 4e), which is referred to as a central ridge feature [*Egli et al.*, 2010]. The central ridge has a peak in the typical range of ~20–60 mT. The switching field distribution for magnetofossil-bearing sediments can extend up to 120 mT [*Roberts et al.*, 2012; *Egli*, 2013].

Table 1. Room Temperature FMR Parameters for the Studied Samples

Samples	Sediment Age and Type	B_{eff} (mT)	g_{eff}	B_{low} (mT)	B_{high} (mT)	ΔB_{low} (mT)	ΔB_{high} (mT)	ΔB_{FWHM} (mT)	A	α
ODP689-11R2-119	Oligocene Pelagic carbonate	336.2	2.00	251.0	397.3	85.2	61.1	146.3	0.717	0.27
DSDP523-26H1-5	Eocene Pelagic carbonate	331.7	2.07	260.0	394.5	71.7	62.8	134.5	0.876	0.28
MD00-2361-315	Glacial carbonate	347.2	2.02	220.4	410.7	126.8	63.5	190.3	0.501	0.27
MD00-2361-655	Glacial carbonate	332.8	2.10	230.4	415.4	102.4	82.6	185.0	0.807	0.32
MD00-2361-1125	Glacial carbonate	345.1	2.03	242.9	417.1	102.2	72.0	174.2	0.705	0.29
MD00-2361-125	Interglacial clay	336.2	2.08	260.0	400.0	76.2	63.8	140.0	0.837	0.28
MD00-2361-1175	Interglacial clay	330.4	2.12	248.4	405.4	82.0	75.0	157.0	0.915	0.31
CD143-55705-01-21	Surface sediment	293.6	2.31	197.9	396.2	95.7	102.6	198.3	1.072	0.38
CD143-55705-01-36	Surface sediment	300.4	2.26	184.9	397.2	115.5	96.8	212.3	0.838	0.35
CD143-55705-01-56	Surface sediment	290.1	2.34	196.5	391.7	93.6	101.6	195.2	1.085	0.38
MD01-2421-01-05	Quaternary marine sediment	307.2	2.26	178.8	392.8	128.4	85.6	214.0	0.666	0.32
MD01-2421-07-50	Quaternary marine sediment	234.5	2.96	150.7	380.5	83.9	146.0	229.8	1.741	0.52
MD01-2421-09-60	Quaternary marine sediment	328.0	2.11	207.8	411.4	120.2	83.4	203.6	0.694	0.32
MD01-2421-09-120	Quaternary marine sediment	331.0	2.09	209.4	408.7	121.6	77.7	199.3	0.639	0.30
MD01-2421-09-140	Quaternary marine sediment	326.7	2.12	188.5	414.5	138.2	87.8	226.0	0.635	0.33
BA8.5	Miocene lake sediments	311.3	2.08	209.3	366.2	102.0	54.9	156.9	0.538	0.25
BA8.54	Miocene lake sediments	317.3	2.04	224.2	371.9	93.1	54.6	147.7	0.586	0.24
BA34	Miocene lake sediments	302.1	2.15	174.8	362.0	127.3	59.9	187.2	0.471	0.26
BG118	Miocene lake sediments	319.9	2.03	219.9	384.9	100.0	65.1	165.1	0.650	0.27
YB-1-29	Quaternary Chinese paleosol	323.0	2.15	231.5	386.2	91.5	63.2	154.7	0.691	0.27
YB-1-59	Quaternary Chinese paleosol	326.0	2.13	236.7	385.4	89.3	59.4	148.7	0.665	0.26
YB-2-20	Quaternary Chinese paleosol	322.9	2.15	220.6	387.5	102.3	64.6	166.9	0.631	0.27
YB-2-50	Quaternary Chinese paleosol	319.4	2.17	221.9	380.2	97.5	60.8	158.3	0.624	0.26
YB-3-11	Quaternary Chinese loess	289.6	2.35	128.6	387.5	161.0	97.9	258.9	0.608	0.36
YB-3-31	Quaternary Chinese loess	274.0	2.53	136.4	391.5	137.6	117.5	255.1	0.854	0.40
YB-3-61	Quaternary Chinese loess	312.9	2.22	164.6	389.6	148.3	76.7	225.0	0.517	0.31
YB-3-81	Quaternary Chinese loess	278.7	2.49	118.3	383.2	160.4	104.5	264.9	0.651	0.37
B90	Quaternary Czech paleosol	307.0	2.11	228.1	375.8	78.9	68.8	147.7	0.872	0.29
TC04_12_01	Tuff	357.2	1.96	254.9	409.3	102.3	52.1	154.4	0.51	0.24
TC04_12_03	Tuff	368.0	1.90	263.9	410.3	104.1	42.3	146.4	0.41	0.21
TC04_11	Tuff	346.6	2.02	201.3	400.8	145.3	54.2	199.5	0.37	0.26
TC04_11	Tuff	354.7	1.97	263.9	410.3	90.8	55.6	146.4	0.61	0.25
TC04_11	Tuff	357.9	1.96	263.9	410.3	94.0	52.4	146.4	0.56	0.24
TC04_11	Tuff	360.3	1.94	263.9	410.3	96.4	50.0	146.4	0.52	0.23
TC04_12_05	Tuff	369.2	1.90	227.6	429.7	141.6	60.5	202.1	0.43	0.27
TC04_12_06	Tuff	350.4	2.00	204.4	430.5	146.0	80.1	226.1	0.55	0.31
TC04_12_07	Tuff	360.1	1.94	202.4	436.9	157.7	76.8	234.5	0.49	0.31
TC04_13_02	Tuff	351.0	2.00	195.2	437.4	155.8	86.4	242.2	0.55	0.33
TC04_14_02	Tuff	365.9	1.91	210.2	439.5	155.7	73.6	229.3	0.47	0.31
TC04_15_03	Tuff	342.9	2.04	207.8	447.2	135.1	104.3	239.4	0.77	0.37
TC05_9.0	Tuff	325.3	2.09	194.8	426.5	130.5	101.1	231.7	0.77	0.36
TC05_7.2	Tuff	328.0	2.07	189.0	427.3	139.0	99.3	238.3	0.71	0.35
TC05_7.1	Tuff	330.5	2.05	184.5	427.0	146.0	96.5	242.5	0.66	0.35

The FMR spectrum for pelagic sediment sample DSDP523-26H1-5 has sharp absorption lines (Figure 5a), as reflected by a line width that is small compared to other samples (Table 1). The intensities of the low- and high-field FMR peaks are similar (Figure 5a). No multiple low-field peaks are observed. There is a possible weak high-field double-well feature (between ~360 and 400 mT). FMR spectra with double peaks at high fields are not widely observed for natural samples. *Chang et al.* [2012b] observed a high-field double-well

Figure 4. Room temperature (a) derivative FMR spectrum, (b) the corresponding FMR absorption spectrum, (c) fitting of the measured FMR spectrum with one biogenic component, (d) fitting of the measured FMR spectrum with two components (biogenic and isotropic), and (e) FORC diagram for a pelagic marine carbonate sample ODP689D-11R2-119 from ODP Site 689, Maud Rise, Weddell Sea, Southern Ocean. These FMR and FORC signatures are typical of samples with biogenic magnetite chains [*Roberts et al.*, 2012, 2013]. In Figure 4a, the FMR spectrum contains multiple peaks (typically two) at low fields (black arrows), a pronounced minimum at high fields (red arrow), and an asymmetric overall shape. This spectrum also contains a weak radical signal with a *g* value of 2 superimposed on the FMR signal. In Figure 4b, definition of FMR parameters is illustrated [*Weiss et al.*, 2004; *Kopp et al.*, 2006a, 2006b]. FMR parameters listed in Figure 4a fall within the $g_{eff} < 2.1$, $A < 1$, and $\alpha < 0.3$ regions. In Figures 4c and 4d, the black line is the measured spectrum, the dotted green line is the biogenic FMR component, the dotted blue line represents an isotropic component, and the dashed red line is the sum of the two model FMR components. This scheme applies to all spectral fits presented in the succeeding figures. Fitted uniaxial anisotropy (B_{uni}) and magnetocrystalline anisotropy (B_{cubic}) are indicated. The FORC diagram in Figure 4e has a central ridge feature [*Egli et al.*, 2010] with negligible vertical spread and peak coercivity of ~30 mT. The thick black line indicates the 0.05 significance level [*Heslop and Roberts*, 2012].
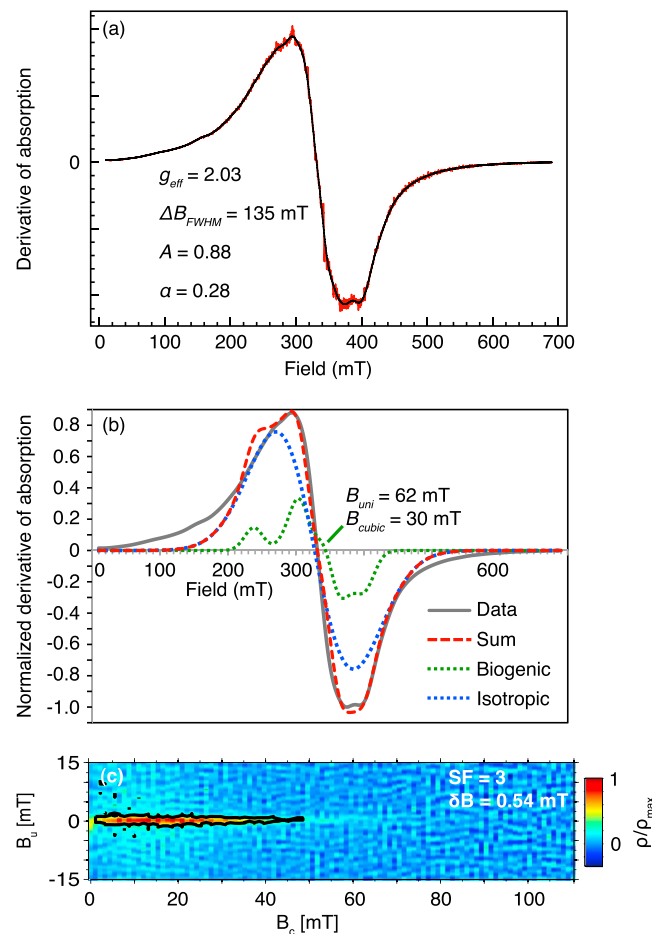
Figure 5. Room temperature (a) FMR spectrum, (b) decomposition of the FMR spectrum with two FMR components, and (c) FORC diagram for a pelagic carbonate sample DSDP523-26H1-5 from DSDP Site 523, South Atlantic Ocean. In Figure 5a, the red curve represents the measured data. The black curve represents smoothed data after fast Fourier transform (FFT) filtering, which removes the high-frequency components [Roberts et al., 2011].

feature for tuff samples with noninteracting titanomagnetite (TM10). The double-well feature is possibly due to spectral superposition. Nevertheless, it is evidently associated with weakly interacting magnetic grains that result in well-resolved FMR peaks. FMR decomposition for this sample also indicates the presence of an isotropic contribution (Figure 5b). A high-resolution FORC diagram for this sample has a central ridge with peak coercivity at ~10 mT (Figure 5c), which is considerably smaller compared to that of typical marine carbonates (Figure 4d) [Roberts et al., 2011, 2012, 2013].

4.2.2. Continental Margin Marine Sediments

4.2.2.1. Western Australian Margin Core MD00-2361

FMR spectra for late Quaternary samples from western Australian margin core MD00-2361 have distinct shapes for glacial (Figure 6a) and interglacial samples (Figure 6b). For glacial samples, all measured EPR spectra contain sharp lines (6 intense and 10 weak lines; dashed area in Figure 6a), which are likely due to Mn^{2+} in calcite [Kopp et al., 2006a]. The Mn^{2+} signal is not of interest here and was removed by fast Fourier transform (FFT) smoothing [Roberts et al., 2011] to isolate parameters that represent only magnetically ordered mineral phases. The smoothed FMR spectrum

contains broader peaks: one at low field and a more pronounced high-field minimum (Figure 6a). The spectra lack the characteristic signatures observed for typical pelagic carbonates that contain dominantly biogenic magnetite, particularly the absence of multiple low-field peaks. FMR parameters for glacial samples are the following: $g_{eff} = 2.02–2.10$, $\Delta B_{FWHM} = 174–190$ mT, $A = 0.50–0.81$, and $\alpha = 0.27–0.32$ (Table 1), which are consistent with those for samples containing magnetofossils [Kopp et al., 2006a, 2006b; Roberts et al., 2011, 2012], despite the different shapes of the FMR spectra. For interglacial samples, there is no obvious Mn^{2+} signal in the EPR spectra (Figure 6b), which is consistent with the fact that these samples are clay rich with low carbonate contents. FMR spectra for interglacial samples contain simple absorption lines with one broad peak at low fields and one minimum at high fields. The spectra are nearly symmetric, as indicated by A values close to 1 (Table 1). Other FMR parameters for interglacial samples are the following: $g_{eff} = 2.08–2.12$, $\Delta B_{FWHM} = 140–157$ mT, and $\alpha = 0.28–0.31$, which are still close to those expected for biogenic magnetite. This is due to the presence of significant biogenic and detrital magnetite components (Figures 3d and 3e) [Heslop et al., 2013]. FMR decomposition indicates that two FMR components, including a biogenic component, can explain the measured spectra (Figures 6c–6f). FORC diagrams for glacial samples contain a dominant central ridge (Figure 6g). Interglacial samples have two major components: a central ridge and a component with lower coercivity and large vertical spread (Figure 6h). The central ridge signature is consistent with the presence of biogenic magnetite within both glacial and
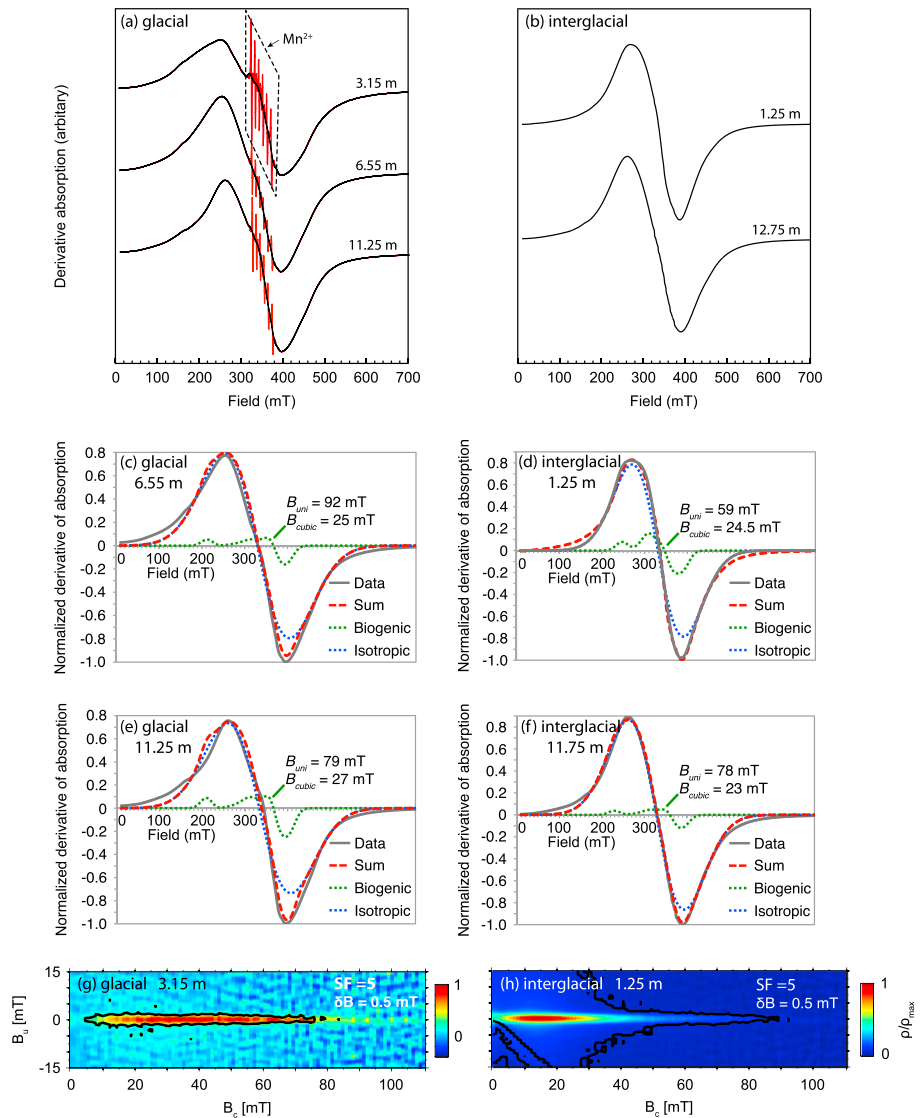
Figure 6. Room temperature (a, b) FMR spectra, (c–f) decomposition of the measured FMR spectra, and (g, h) FORC diagrams for continental margin marine sediment samples from core MD00-2361 offshore of Western Australia. Carbonate-rich glacial samples (Figures 6a, 6c, and 6e). Clay-rich interglacial samples (Figures 6b, 6d, and 6f).

interglacial samples (Figures 3a and 3b), while the component with vertical spread is due to a coarser-grained detrital component [*Heslop et al.*, 2013].

4.2.2.2. Oman Margin Core CD143-55705

FMR spectra for surface sediments from Oman Margin core CD143-55705 have broad background absorption lines and sharp Mn^{2+} lines (Figures 7a–7c). The spectra lack characteristic biogenic magnetite signatures (Figure 4a). Large g_{eff} values (~2.3), large ΔB_{FWHM} values (~200 mT), $A > 1$, and large α values (0.35–0.38) (Table 1) all deviate significantly from those expected for biogenic minerals. Decomposition of the FMR spectra indicates a dominant symmetric contribution in experimental spectra, which makes definition of a meaningful biogenic component problematic (Figures 7d–7f). FORC diagrams indicate two components: a central ridge FORC signature with peak coercivity at ~15–30 mT, and a FORC distribution that spreads along the vertical axis (Figures 7g–7i). This central ridge FORC component is typical of biogenic magnetite (cf. Figures 4b and 6d–6f) [*Egli et al.*, 2010; *Roberts et al.*, 2012]. The other FORC component with significant vertical spread is characteristic of samples containing pseudo-single domain (PSD)/multidomain (MD) grains [*Roberts et al.*, 2000; *Pike et al.*, 2001b] probably from detrital magnetite [*Rowan et al.*, 2009].
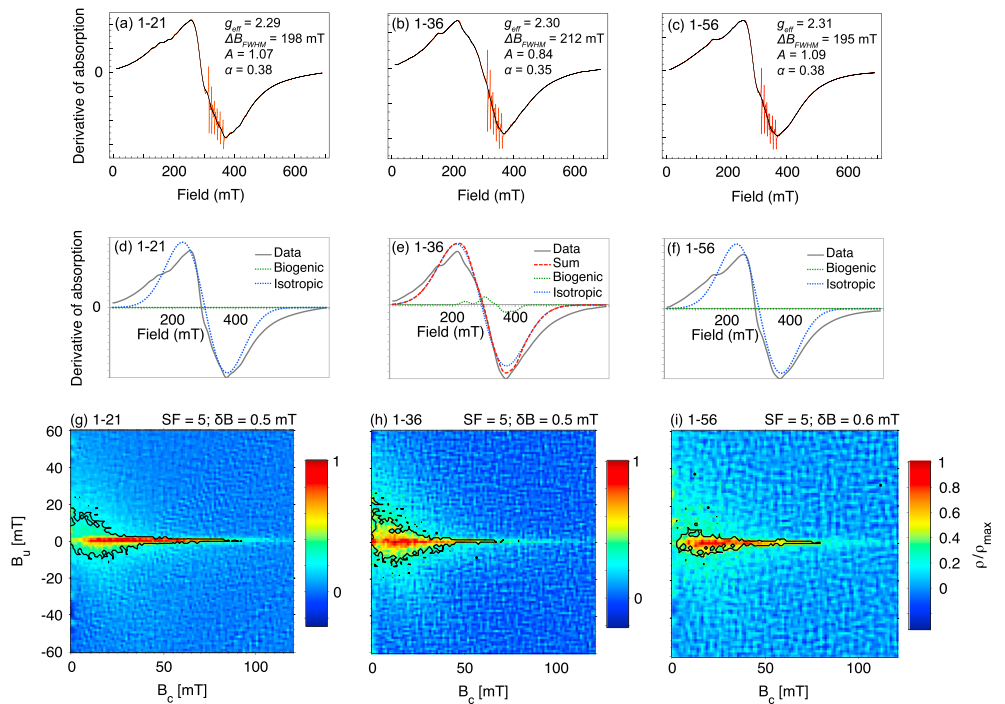
Figure 7. Room temperature (a–c) FMR spectra, (d–f) decomposition of the measured FMR spectra, and (g–i) FORC diagrams for several surface marine sediment samples from core CD143-55705 from the Oman margin, northwestern Arabian Sea. In Figures 7a–7c, the red lines represent the original measured data. Black lines are after FFT smoothing. In Figures 7d and 7f, the decomposition of all three experimental FMR spectra from the automatic fitting program is not satisfactory. Please refer to text for discussion.

4.2.2.3. Core MD01-2421, Northwest Pacific Ocean Offshore of Central Japan

FMR spectra for selected samples from core MD01-2421 have diverse characteristics (Figures 8a–8d). Some FMR spectra contain a broad low-field peak, and/or multiple small peaks, and a high-field trough (Figures 8a, 8c, and 8d), with relatively low g_{eff} (~2.1), A (~0.6–0.7), and α values ~0.3 (Table 1). Compared to biogenic magnetite (Figure 4a), samples from core MD01-2421 have broader absorption lines (Figures 8a–8d). FMR spectra for many other samples from core MD01-2421 are complex, particularly at low fields (Figure 8b). These samples have large g_{eff}, A, and α values (Table 1), which probably reflect contributions from mixtures of magnetic minerals and domain states. The central ridge FORC components have peak coercivities at ~10–40 mT. Some samples have a high coercivity
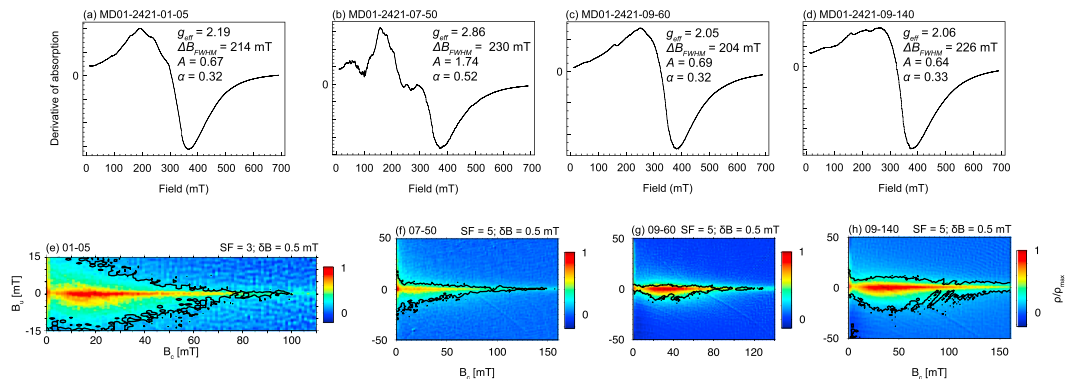

Figure 8. Room temperature (a–d) FMR spectra and (e–h) FORC diagrams for continental margin marine sediments from core MD01-2421 offshore of central Japan, north Pacific.
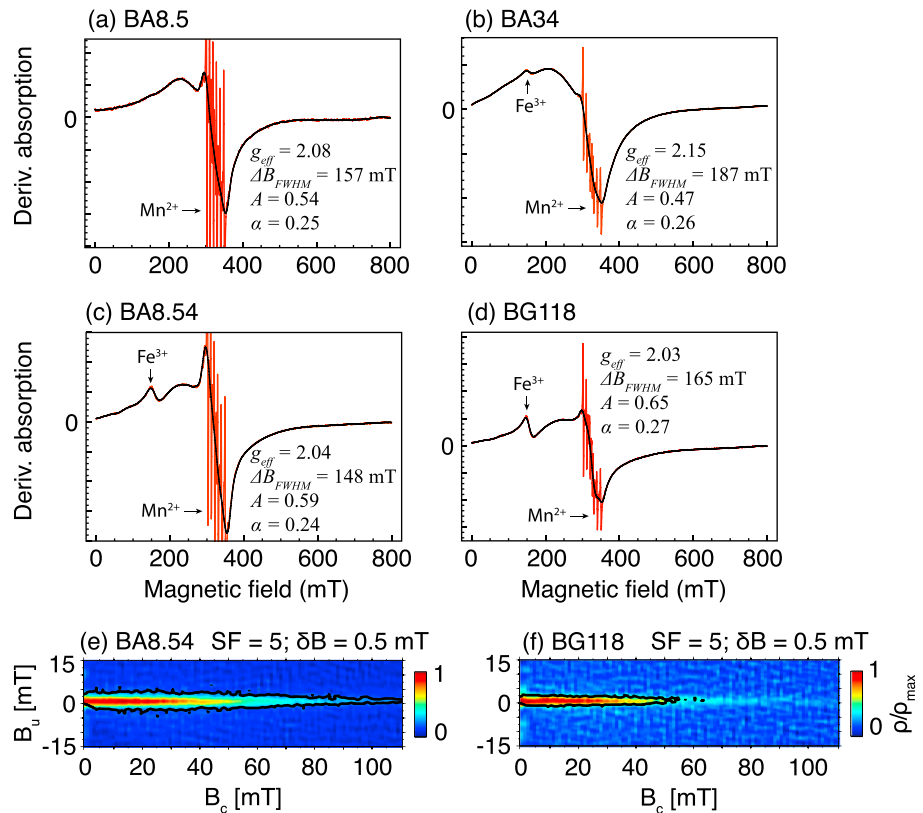
Figure 9. Room temperature (a–d) FMR spectra and (e, f) FORC diagrams for a range of lake sediment samples from the DLS, Europe (see Figure 1). Black lines are the smoothed data using FFT filtering. The sharp red lines (at ~310–380 mT) originate from paramagnetic Mn^{2+}.

tail associated with the central ridge that extends to >160 mT (Figures 8f–8h). This probably indicates much broader magnetic particle size distributions, compared to those for biogenic magnetite. The "teardrop" shaped FORC distributions indicate that some particles are magnetostatically interacting (Figures 8e–8h) [*Egli et al.*, 2010; *Kind et al.*, 2011; *Li et al.*, 2012].

4.3. Lake Sediments, Dinaride Lake System

FMR spectra for the DLS sediments (Figures 9a–9d) have a peak at $g = 4.3$ due to paramagnetic high-spin Fe^{3+}, and a Mn^{2+} sextet signal. All samples have double low-field peaks (not taking into account the Fe^{3+} peak) and a pronounced high-field minimum (Figures 9a–9d). FMR parameters for these samples are the following: $g_{eff} = $ ~2.04–2.15, $\Delta B_{FWHM} = 148$–187 mT, $A < 1$ (~0.47–0.65), and $\alpha < 0.3$ (0.24–0.27). These FMR signatures are consistent with the expectations for biogenic magnetite [e.g., *Weiss et al.*, 2004; *Kopp et al.*, 2006a, 2006b; *Charilaou et al.*, 2011a; *Chang et al.*, 2012b], as are the FMR parameters [*Kopp et al.*, 2006a, 2006b, 2007; *Roberts et al.*, 2011, 2012]. FORC diagrams for all measured DLS samples contain a dominant central ridge (Figures 9e and 9f).

4.4. Chinese and Czech Loess and Paleosols

FMR spectra for selected Chinese paleosol samples contain a low-intensity peak at low fields and a relatively pronounced high-field peak at ~360 mT (Figure 10a). The low-field peak is broad with a plateau between ~250 and 280 mT, with $g_{eff} = $ ~2.13–2.17, $A = $ ~0.6–0.7, and $\alpha < 0.3$ (Table 1). Compared to Chinese paleosol samples, much more complex FMR spectra are observed for loess samples with large variations in shape, particularly at low fields (Figure 10b). The loess samples have large g_{eff} (2.22–2.53), ΔB_{FWHM} (225–365 mT), and α values (0.31–0.40) (Table 1). This probably reflects the properties of detrital magnetic particles, with broad particle size distributions and PSD behavior. FORC diagrams of Chinese paleosol samples are indicative of two dominant components (Figure 10c). One has small vertical spread with peak coercivity at ~10 mT, which indicates weak magnetostatic interactions. This FORC central ridge component is probably due to
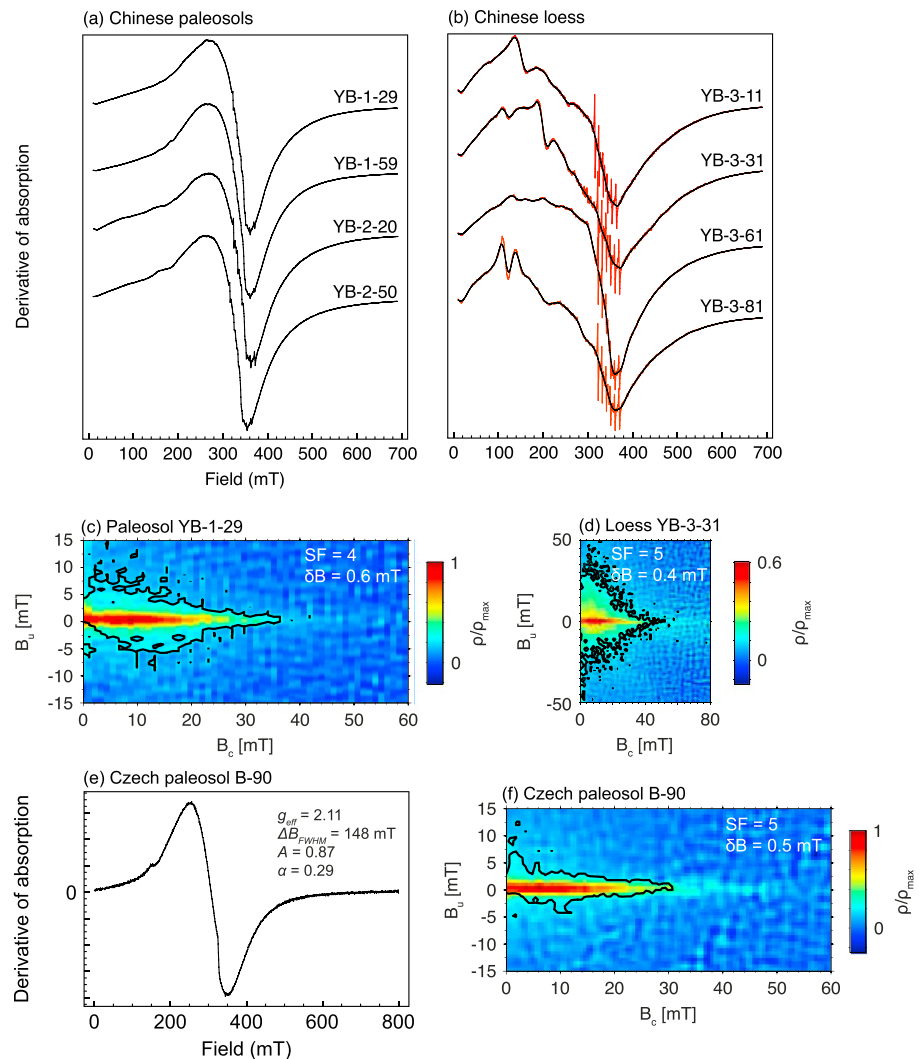
Figure 10. Room temperature (a, b) FMR spectra and (c, d) FORC diagrams for samples from Chinese loess/paleosol samples: paleosol samples (Figures 10a and 10c) and loess samples (Figures 10b and 10d). (e) FMR spectrum and (f) FORC diagram for paleosol sample B-90 from the Southern Czech Republic. In Figure 10b, red lines represent the original measured data; black lines are after FFT smoothing.

authigenically precipitated noninteracting pedogenic magnetite [*Geiss et al.*, 2008]. The other component has a FORC distribution that is spread along the vertical axis, which is characteristic of samples containing PSD/MD magnetite [*Roberts et al.*, 2000; *Pike et al.*, 2001b; *Muxworthy and Dunlop*, 2002]. This type of FORC diagram (Figure 10c) has been observed for other paleosol samples [*Geiss et al.*, 2008]. In contrast, FORC distributions for loess samples are noisy, but spread toward the vertical axis without a clear central ridge signature (Figure 10d).

A FMR spectrum for a paleosol sample from the southern Czech Republic has narrow absorption lines (Figure 10e) compared to samples with strong magnetostatic interactions [e.g., *Weiss et al.*, 2004; *Kopp et al.*, 2006a, 2006b; *Chang et al.*, 2012b]. The spectrum is consistent with those observed for SD magnetite [*Valstyn et al.*, 1962]. The sample has $g_{eff} = 2.11$, $\Delta B_{FWHM} = 148$ mT, $A = 0.87$, and $\alpha = 0.29$. A FORC diagram (Figure 10f) represents a superposition of two components: a central ridge with peak coercivity at ~8 mT and a distribution with vertically spread close to $B_c = 0$ [*van Oorschot et al.*, 2002].

4.5. TC Tuff

FMR spectra for all studied TC tuff samples contain well-resolved absorption lines. For example, there are multiple peaks at low and high fields (Figures 11a–11l), unlike typical FMR spectra for natural inorganic
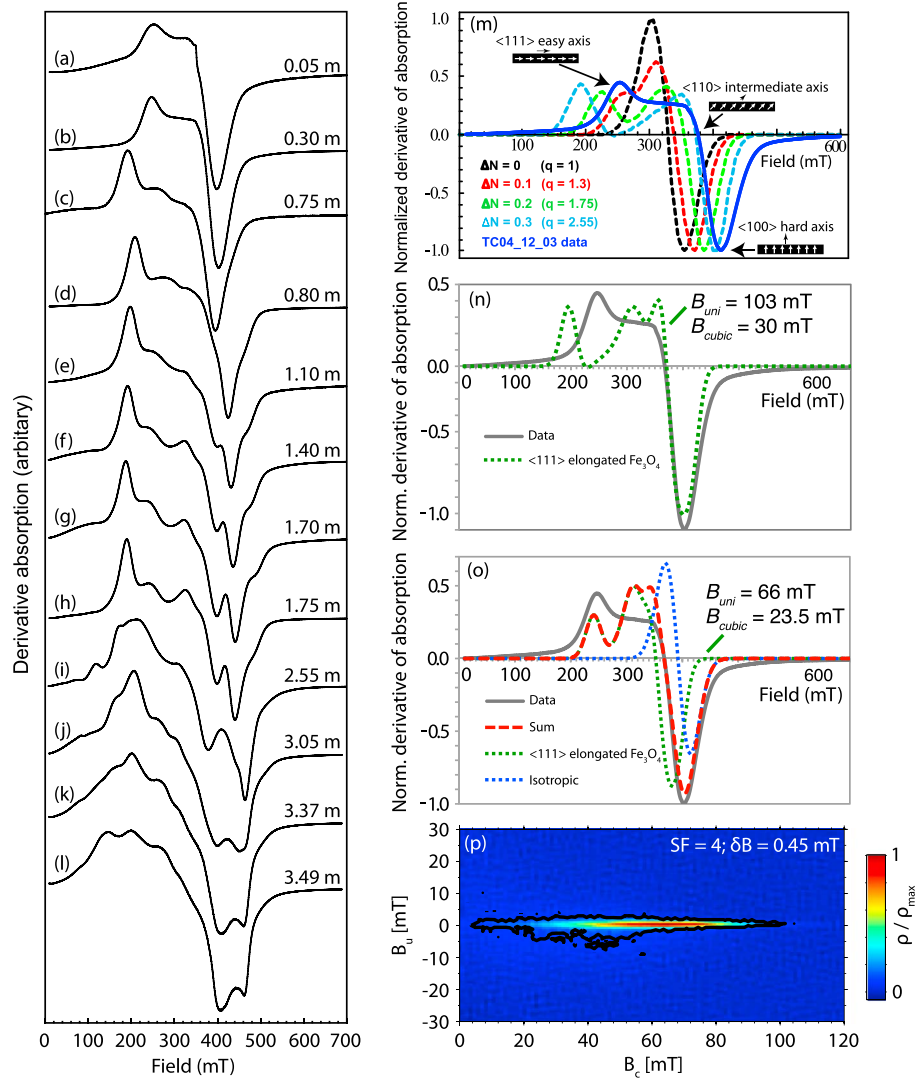
Figure 11. Room temperature (a–l) FMR spectra, (m–o) theoretical FMR spectra analysis, and (p) FORC diagram for TC tuff samples. Stratigraphic levels are indicated for each sample (Figures 11a–11l). Comparison of a measured X-band FMR spectrum for sample "TC04_12_03" (at a height of 0.30 m in the TC tuff cooling unit) and simulated FMR spectra for unoriented and isolated SD magnetite crystals with different degrees of elongation along the <111> crystallographic axis (Figure 11m). All FMR spectra are normalized to the minimum value. ΔN represents the effective demagnetization factors, and q is the axial ratio (length/width). Best fits of the measured FMR spectrum for sample TC04_12_03 are shown in Figure 11n with one component for magnetite crystals with elongation along the <111> direction, and in Figure 11o with two components (an isotropic spectrum and an asymmetric spectrum for magnetite crystals with <111> elongation). Large deviations between simulations and experimental data probably indicate that the TC tuff samples do not have ideal crystallographic elongation along the <111> axis.

samples with only one low-field maximum and one high-field minimum [*Weiss et al.*, 2004; *Kopp et al.*, 2006a; *Fischer et al.*, 2007; *Chang et al.*, 2012b]. FMR parameters for the TC tuff samples (Table 1) are also significantly different from those of natural samples with strong magnetostatic interactions [*Weiss et al.*, 2004; *Chang et al.*, 2012b]. For example, most measured TC tuff samples have much reduced g_{eff}, A, ΔB_{FWHM}, and α values. With increasing stratigraphic level, we observe a continuous change in FMR spectra (Figures 11a–11l). Samples from the base of the studied section (i.e., at 0.05 and 0.30 m), which contain magnetic minerals with composition close to magnetite and dominantly SP behavior, have strongly asymmetric FMR spectra with two low-field peaks and one pronounced high-field minimum (Figures 11a and 11b). The sample at 0.75 m also has an asymmetric FMR spectrum, but with three low-field peaks and one pronounced
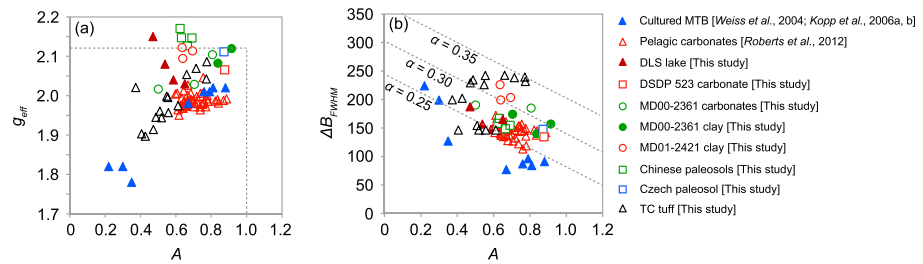
Figure 12. Plots of FMR parameters in a (a) g_{eff} versus A diagram and a (b) ΔB_{FWHM} versus A diagram [*Weiss et al.*, 2004; *Kopp et al.*, 2006a, 2006b]. The dashed lines in Figure 12a represent $g_{eff} = 2.12$ and $A = 1$. Data from MTB fall within the region with $A < 1$ and $g_{eff} < 2.12$ [*Weiss et al.*, 2004; *Kopp et al.*, 2006a, 2006b]. The dashed lines in Figure 12b are contours of the empirical FMR parameter α (see text for a description of α). FMR parameters for several samples that contain a significant amount of detrital magnetic mineral grains are not plotted because their FMR parameters deviate significantly from the region expected for biogenic magnetite.

high-field peak (Figure 11c). Samples from above 1.40 m have several low-field peaks (≥3) and multiple (mostly two) high-field peaks (Figures 11f–11l). We performed spectral fitting of one simpler FMR spectrum of sample "TC04_11_03" (at 0.30 m; Figures 11m–11o). A typical FORC diagram for a SD TC tuff sample ("TC05_7.1"; at 3.49 m) indicates a dominant central ridge component with peak coercivity at ~60 mT (Figure 11p). This central ridge originates from noninteracting SD grains. Another minor component with lower coercivity and moderate vertical spread due to interacting grains is also visible (Figure 11p).

5. Discussion

5.1. FMR and FORC Signatures of Biogenic Magnetite in Sedimentary Environments

We have tested the usefulness of FMR and FORC analyses for identifying biogenic magnetite in samples from diverse sedimentary environments (Figures 4–9). These analyses are constrained by TEM observations (Figure 3) and coercivity analysis of IRM acquisition curves (supporting information). Below we evaluate these results in terms of biogenic magnetic mineral signatures.

5.1.1. Sediments Rich in Biogenic Magnetite

Positive identifications of biogenic magnetite signatures from sediment samples using both FMR and FORC analyses are not yet common. For the studied samples, only some pelagic carbonates (Figure 4) have strongly positive tests from both methods. These samples typically have the following: (a) asymmetric FMR spectra with absorption extended to low fields, clear multiple low-field peaks and a pronounced high-field trough (Figure 4a), and FMR parameters within the region of $g_{eff} < 2.1$, $A < 1$, and $\alpha < 0.3$ (Table 1 and Figure 12) [e.g., *Weiss et al.*, 2004; *Kopp et al.*, 2006a, 2006b]; and (b) FORC diagrams with a dominant central ridge signature with peak switching field in the ~20–60 mT range (Figure 4b). Central ridge coercivity spectra often have a skewed distribution [e.g., *Egli et al.*, 2010; *Ludwig et al.*, 2013; *Roberts et al.*, 2013; *Heslop et al.*, 2014]. The fact that both FMR and FORC analyses give positive identifications strongly suggests the presence of biogenic magnetite. This is consistent with TEM images of abundant biogenic magnetite crystals. Coercivity distributions from IRM acquisition curves have a dominant component with small values [e.g., *Kruiver and Passier*, 2001] of the dispersion parameter (DP) of *Robertson and France* [1994] (supporting information), which are also consistent with the presence of biogenic magnetite.

Although samples that are rich in biogenic magnetite often give positive tests from both FMR and FORC analyses, this is not always the case. Pelagic marine carbonates from DSDP site 523 (Figure 5) have been demonstrated to contain significant amounts of biogenic magnetite [*Petersen et al.*, 1986; *Vali et al.*, 1987]. However, we do not observe the characteristic FMR signatures expected for biogenic magnetite, as is commonly observed for other pelagic carbonates [*Roberts et al.*, 2011, 2012, 2013; *Larrasoaña et al.*, 2012]. A FORC diagram for this sample contains a dominant central ridge (Figure 5b), but the peak coercivity of the central ridge is relatively low (~10 mT) compared to typical intact biogenic magnetite samples [*Pan et al.*, 2005; *Chen et al.*, 2007; *Li et al.*, 2009, 2010; *Lin and Pan*, 2009; *Roberts et al.*, 2012; *Ludwig et al.*, 2013]. This is probably due to significant collapsing of magnetosome chains, which will not give rise to strongly asymmetric FMR spectra [*Kopp et al.*, 2006a, 2006b] and will also decrease the peak coercivity compared to intact magnetosomes. This is confirmed by our FMR decomposition (section 5.2). Similarly, we did not

observe strongly characteristic biogenic FMR spectra (Figures 9a–9d) for the studied lake sediments, although FMR parameters do fall within the region for intact biogenic magnetite (Figure 12) and FORC diagrams confirm a dominant central ridge (Figures 9e and 9f). These FMR spectra have multiple low-field peaks (Figures 9a–9d), but do not necessarily reflect the presence of intact magnetosomes. The FMR spectra contain a nearly symmetric narrow signal with $g = {\sim}2$ (Figures 9a and 9c). This narrow FMR feature is indicative of SP particles and when superimposed on the broader FMR spectrum can produce the observed multiple low-field peaks. This interpretation is consistent with a lower coercivity peak for the FORC central ridge (Figure 9e). The presence of SP particles is also confirmed by room temperature AC susceptibility measurements that indicate strong frequency dependence and wasp-waisted hysteresis loops [*Roberts et al.*, 1995; *Tauxe et al.*, 1996].

5.1.2. Sediments Containing Mixtures of Biogenic and Nonbiogenic Magnetic Minerals

Mixed magnetic mineral assemblages are much more common than sediments that contain only a single magnetic mineral component. In continental margin environments, multiple terrigenous sediment sources, biogenic particles, and inorganic authigenic magnetic sulfide minerals can give rise to complex magnetic signatures. Unsurprisingly, our FMR and FORC analyses of continental margin sediments often reveal complex results (Figures 6–8). FMR spectra of surface sediments from core CD143-55705 on the Oman margin [*Rowan et al.*, 2009] contain no evidence of biogenic magnetite signatures (Figures 7a–7c and 11 and Table 1), but a biogenic signature is present as a FORC central ridge feature (Figures 7g–7i).

A similar situation exists for Quaternary samples from core MD00-2361, offshore of Western Australia. TEM observations indicate abundant biogenic magnetite within these samples (Figures 3b–3e). FMR spectra for interglacial samples have nearly symmetric lines that do not indicate a clear biogenic signature (Figure 6b), while FORC diagrams for the same samples contain a strong central ridge signature (Figure 6h). Glacial samples from this core contain abundant biogenic magnetite (Figures 3b and 3c), which is consistent with a dominant central ridge FORC signature (Figure 6g). Unlike the strongly positive test from FORC analysis, FMR results for glacial samples do not reveal a strong biogenic signature. Compared to interglacial samples, FMR spectra for glacial samples have a more asymmetric shape and a more pronounced high-field peak. Their FMR parameters also shift toward the region expected for biogenic magnetite (Table 1 and Figure 12). Our FMR decomposition (section 5.2) indicates that these FMR spectra are a superposition of a symmetric component (probably due to collapsed magnetosome chains and detrital magnetic minerals) and an asymmetric FMR component due to intact biogenic magnetite (Figures 6c–6f).

5.1.3. Sediments With Negligible Biogenic Magnetite Concentrations

FMR spectra and FORC diagrams are compared for sediments that lack significant biogenic magnetite concentrations. For samples from core MD01-2421, offshore of central Japan, dominant IRM components have large DP values (>0.3; supporting information), which reflect magnetic mineral assemblages with a broad coercivity distribution. Their magnetic properties, therefore, appear to be dominated by detrital minerals. However, FORC and FMR signatures partially overlap with those for biogenic samples. FORC diagrams have relatively small vertical spread associated with weak magnetostatic interactions (Figures 8e–8h). Some FMR spectra have multiple peaks at low fields, relatively asymmetric shapes with a more pronounced high-field peak, and lower g_{eff}, A, and α (Figure 8 and Table 1). These FMR features are probably due to superposition of different features and do not necessarily indicate the presence of intact biogenic magnetite chains.

Similar phenomena are observed for FMR spectra from Chinese and Czech paleosols, which contain narrow absorption lines that reflect weak magnetostatic interactions. This is consistent with a FORC central ridge signature. The FMR and FORC signatures are unlikely to be due to biogenic magnetite because the FMR spectra do not indicate a strong shape anisotropy due to magnetosome chains (Figure 10a) and the peak central ridge coercivity (Figure 10c) is low compared to typical intact magnetosome samples. Instead, the FMR and FORC signatures indicate noninteracting mineral grains, which is consistent with knowledge that pedogenesis gives rise to chemical precipitation of relatively isolated magnetic particles [*Geiss et al.*, 2008]. This is also consistent with the completely different FMR and FORC signatures of Chinese loess samples that lack signatures produced by pedogenic magnetic particles (Figures 10b and 10d).

5.2. Recognition of Biogenic Magnetite Signatures From FMR Spectral Decomposition

FMR and FORC measurements on the same biogenic magnetite-bearing samples from diverse sedimentary environments indicate that FORC central ridges provide a more sensitive signature for detecting biogenic
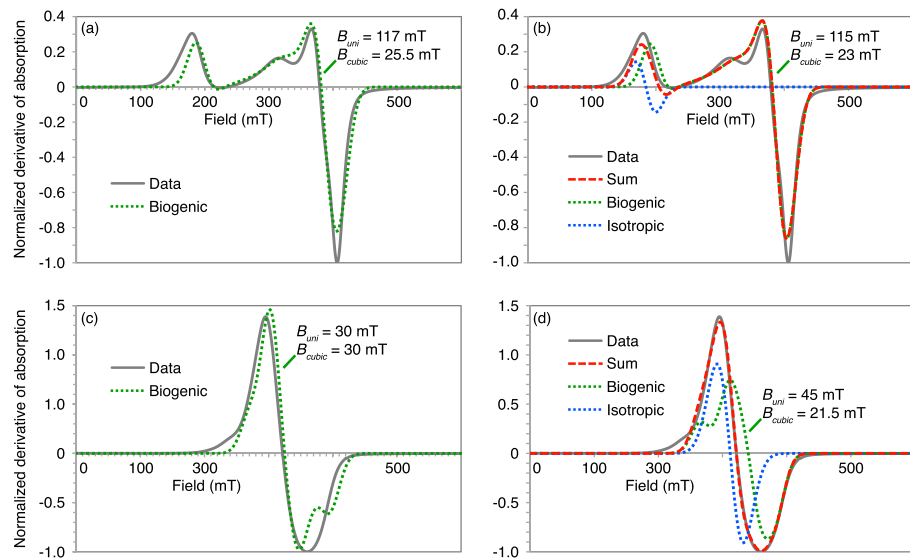
Figure 13. FMR decomposition for two cultured MTB samples with pure biogenic magnetite: (a, b) MTB strain MV-1 and (c, d) mutant (*mnm18*) MTB strain AMB-1. Experimental FMR spectra are from *Kopp et al.* [2006a]. Strain MV-1 typically produces chains of elongated hexa-octahedral magnetite. Mutant *mnm18* of AMB-1 produces nearly equidimensional crystals with both isolated magnetite and magnetite in short chains. In Figures 13a and 13c, the experimental FMR spectra are shown along with a single biogenic component. In Figures 13b and 13d, fitted spectra include a biogenic component and an isotropic component and their sum.

magnetite. This is because the FORC central ridge is uniquely selective of noninteracting SD particles. Our TEM observations unambiguously confirm the presence of biogenic magnetite crystals (Figure 3). Biogenic magnetite chains should enhance the shape anisotropy, and therefore, make characteristic contributions to FMR spectra. While the shape of FMR spectra and derived FMR parameters are useful indicators of biogenic particles, care is often needed due to ambiguities associated with their interpretation. Diagnostic FMR parameters provide key information to identify and characterize biogenic magnetite-bearing samples [e.g., *Weiss et al.*, 2004; *Kopp et al.*, 2006a, 2006b, 2007, 2009; *Maloof et al.*, 2007; *Roberts et al.*, 2011, 2012, 2013; *Larrasoaña et al.*, 2012; *Chang et al.*, 2012b, 2013; *Kodama et al.*, 2013]. However, for complex natural samples with multiple magnetic mineral components (i.e., mixtures of magnetic minerals, grain sizes, domain states, and anisotropies), significant spectral superposition is anticipated. This is a common problem when using bulk magnetic parameters from natural samples. Therefore, for magnetically mixed samples, additional analyses are needed, such as spectral decomposition [*Kopp et al.*, 2006a, 2006b; *Maloof et al.*, 2007], or FMR measurements at low temperatures or at different bands [*Gehring et al.*, 2012, 2013].

The FMR spectrum for a typical magnetofossil-bearing marine carbonate (Figure 4) probably represents an extreme example of natural sediment rich in magnetofossils, although it contains other magnetic components, such as collapsed magnetite chains and detrital magnetic minerals. Therefore, FMR analysis of cultured MTB samples is presented as an ideal case of intact biogenic magnetite chains (Figure 13). Using the model of *Charilaou et al.* [2011a], the spectrum for cultured MTB strain MV-1 can be explained by a single FMR component (Figure 13a) [*Kopp et al.*, 2006a, 2006b; *Charilaou et al.*, 2011a, 2011b]. Adding FMR components does not significantly improve the fit (Figure 13b). Similar analysis of mutant (*mnm18*) MTB strain AMB-1 indicates that two FMR components provide a superior fit, which is probably because this strain contains both isolated magnetosome crystals and magnetite in short chains [*Kopp et al.*, 2006a].

FMR decomposition results for the studied samples are presented alongside experimental FMR spectra and FORC data (Figures 4c, 4d, 5b, and 6c–6f). We only considered binary mixtures with one biogenic magnetite and one isotropic FMR component. This is a simplification: in nature, biogenic magnetite in sediments is produced by different MTB strains, with variable crystal morphologies and chain configurations. These variations result in a range of shape anisotropies and, therefore, should be approximated by multiple biogenic components. Similarly, the isotropic component will also potentially have multiple origins, such as

collapsed magnetosome crystals and detrital magnetic particles, which will cause deviations from simple binary mixtures. In addition, the model of *Charilaou et al.* [2011b], which we use to create the theoretical biogenic FMR component, assumes an ellipsoidal morphology for biogenic magnetite chains. This approach can explain many experimental FMR features observed for cultured MTB samples, but deviations between model simulations and experimental data still occur [*Charilaou et al.*, 2011a].

We also built more complex models to decompose FMR spectra for samples that contain biogenic magnetite. For example, we fitted experimental FMR spectra with one symmetric component and two biogenic magnetite components to represent "biogenic soft" and "biogenic hard" magnetite [*Egli*, 2004a]. We also simulated biogenic magnetite components with a distribution of FMR parameters, rather than using fixed values to better represent natural samples. These modified biogenic components were then fitted to FMR spectra for natural samples. Finally, we considered oxidation of biogenic magnetite, which is common for magnetofossil-bearing samples [*Smirnov and Tarduno*, 2000; *Chang et al.*, 2013]. Magnetite oxidation affects the resonance conditions (i.e., lower saturation magnetization and lower magnetocrystalline anisotropy) and g value, which will shift the FMR spectrum. This effect was simulated and tested in the FMR fittings. Results of these more complex FMR fitting models only slightly improve the simpler binary model. We, therefore, use the simpler model in this paper.

Despite simplifying assumptions, the experimental FMR spectra can be fitted reasonably well with two components: an asymmetric component for intact biogenic magnetite chains and an isotropic component. The magnetofossil-bearing pelagic carbonate from ODP 689 has a larger contribution from intact biogenic magnetite chains compared to the pelagic sediment from DSDP 523, which probably contains a larger amount of collapsed biogenic magnetite chains. This is also consistent with bulk FMR and FORC measurements and is confirmed by the fitted physical parameters (i.e., uniaxial anisotropy). The ODP 689 sample contains a component with a larger fitted shape anisotropy (better chain configuration) compared to the DSDP 523 sample. For glacial and interglacial samples from offshore of Western Australia, a good fit is generally obtained with FMR components. This is consistent with the FORC measurements and TEM observations that indicate the presence of biogenic and detrital components. For the Oman margin surface sediment samples, it is difficult to fit FMR spectra with intact biogenic magnetite. This is probably because the samples contain a significant nonbiogenic component or collapsed biogenic magnetite chains. Our FMR fitting for a large set of magnetofossil-bearing samples indicates that a strong biogenic signature is not common for natural samples. This probably indicates that magnetofossils in many natural environments are not well preserved as intact chains with a <111> orientation. Collapse of biogenic magnetite chains reduces chain-induced anisotropy, which smears the characteristic signature observed for cultured MTB samples [*Kopp et al.*, 2006b]. This makes it difficult to extract biogenic magnetite signatures using FMR spectroscopy for natural samples with collapsed magnetofossil chains.

5.3. Are FMR Signatures for Biogenic Magnetite Unique?

Characteristic asymmetric FMR spectra with multiple low-field peaks and a pronounced high-field minimum are known only for intact magnetosome chains [e.g., *Weiss et al.*, 2004; *Kopp et al.*, 2006a, 2006b, 2007; *Fischer et al.*, 2008; *Roberts et al.*, 2012]. The g_{eff} values < 2 have not been reported for natural samples containing inorganic magnetic minerals. Our FMR measurements indicate that some TC tuff samples (Figure 11) share characteristics with biogenic magnetite, with FMR parameters that fall within the expected range (Table 1). Experimental and theoretical analyses confirm that asymmetric FMR spectra are due to a combination of strong shape anisotropy and absence of magnetostatic interactions [e.g., *Weiss et al.*, 2004; *Kopp et al.*, 2006a, 2006b; *Chang et al.*, 2012b]. An intact magnetosome chain behaves like an isolated uniaxial stable SD grain [*Moskowitz et al.*, 1993; *Penninga et al.*, 1995; *Dunin-Borkowski et al.*, 1998]. The TC tuff samples have strong shape anisotropy and lack magnetostatic interactions [*Worm and Jackson*, 1999; *Roberts et al.*, 2000; *Pike et al.*, 2001a] because the magnetic particles are elongated and dispersed within the tuff matrix [*Schlinger et al.*, 1991]. This can explain the general similarities of FMR spectra for intact biogenic magnetite and TC tuff samples, i.e., reduced g_{eff} and multiple sharp absorption lines.

There are also noticeable differences among FMR spectra for the TC tuff samples (Figure 11). Different grain size distributions should not produce significantly different FMR spectra. FMR simulations indicate that characteristic spectra for biogenic magnetite originate from alignment of magnetosomes along the <111> crystallographic axis of magnetite (or grain elongation along the easy axis <111>) [*Charilaou et al.*, 2011a].

FMR simulations of magnetic particles with elongation along different crystallographic axes produce significantly different FMR spectra. These simulations also indicate that mixed crystal elongations can roughly explain key features of FMR spectra for the TC tuff samples, i.e., the double-well high-field minima [*Chang et al.*, 2012b]. Elongation of magnetic crystals along different directions, therefore, probably makes a significant contribution to the observed differences in FMR spectra among the TC tuff samples. It is possible that progressively changing volcanic conditions produced crystallization of magnetic minerals along different preferred directions. Samples from the base of the TC tuff section (Figures 11a–11c) have FMR features that are more similar to those of biogenic magnetite. Slightly increasing Ti content, which would change the magnetocrystalline anisotropy, may also contribute to the generally more complex FMR signatures for samples from higher levels. We compare the FMR spectrum for sample TC04_12_03 with simulated FMR spectra (Figure 11m). These spectra share similar features, i.e., double low-field peaks and a pronounced high-field minimum. Increasing particle elongation (and, therefore, increasing shape anisotropy) shifts the high-field minimum to higher fields. The experimental high-field minimum at ~410 mT and much reduced g_{eff} value (1.90) for sample TC04_12_03 should, therefore, correspond to magnetic mineral assemblages with significant elongation (i.e., $q > 2.55$) using the approach of *Charilaou et al.* [2011a], which is consistent with TEM observations (samples around this level have q between ~3.57 and 5.00 [*Schlinger et al.*, 1991]). However, the low-field peaks for sample TC04_12_03 occur at higher fields compared to simulations of magnetic mineral assemblages with elongation along the <111> direction. In addition, a single model component with <111> elongation cannot fully explain the measured FMR spectrum; for example, the fitted spectrum has a similar g value as experimental data but there are significant deviations in the low- and high-field peaks (Figure 11m). After adding an isotropic component for sample TC04_12_03 in addition to a magnetite component with elongation along the <111> direction (Figure 11n), the fit improves slightly in terms of both the g value and the high-field branch. The low-field peaks are also broadly consistent with the measured data, with some discrepancies in peak intensity (Figure 11n). Our analysis confirms that the TC tuff samples can have similar FMR characteristics, e.g., general spectral shape and parameters. However, inorganic magnetite with elongation that is not along the <111> direction makes them distinguishable from intact biogenic magnetite chains.

Our experimental data from TC tuff samples confirm that characteristic FMR spectra for biogenic magnetite are due to a combination of chain assembly and isolation of individual magnetosome chains [*Weiss et al.*, 2004; *Kopp et al.*, 2006a, 2006b]. More importantly, our data indicate that FMR spectroscopy does not necessarily provide unique identification of biogenic magnetic minerals because overlaps in both FMR shape (Figure 11) and parameters (Figure 12) are possible for biogenic and abiogenic magnetic minerals. FORC diagrams with a central ridge have also been widely documented for nonbiogenic magnetic particles [e.g., *Pike et al.*, 1999; *Roberts et al.*, 2000, 2006; *van Oorschot et al.*, 2002; *Geiss et al.*, 2008], and reflect SD magnetic particle systems with negligible magnetostatic interactions [*Pike et al.*, 1999; *Roberts et al.*, 2000; *Egli et al.*, 2010], and not necessarily only intact magnetosome chains. Natural inorganic processes can produce magnetic mineral assemblages with similar characteristics to those of biogenic magnetite. For example, magnetic particles produced by volcanism can be transported from source and deposited in sediments and can produce a FORC central ridge, which resembles those due to biogenic magnetite [*Ludwig et al.*, 2013]. While the special magnetic properties of the TC tuff samples are unlikely to be widely replicated in sediments where the magnetic properties are more likely to have a contribution from biogenic magnetic minerals, our results should be borne in mind when using FMR spectroscopy to identify biogenic magnetite.

5.4. Toward a Robust and Efficient Protocol for Identifying Biogenic Magnetite

Like all other magnetic methods for identifying biogenic minerals, FMR and FORC analyses have advantages and limitations. The most distinctive advantage of FMR spectroscopy is that it is not only sensitive to varying domain state and magnetostatic interactions (for detecting separation of biogenic magnetite chains within the sediment matrix), but to magnetic anisotropy (for detecting the chain assembly of biogenic magnetite along the <111> crystallographic axis). These properties produce sharp, asymmetric, and characteristic spectra that are not commonly shared with inorganic magnetic minerals. This makes FMR analysis an extremely powerful tool for recognizing intact biogenic magnetite chains compared to all other magnetic methods. A positive FMR test means that time-consuming TEM and additional magnetic analyses are probably unnecessary. This will significantly improve search efficiency. FMR spectroscopy is also sensitive to
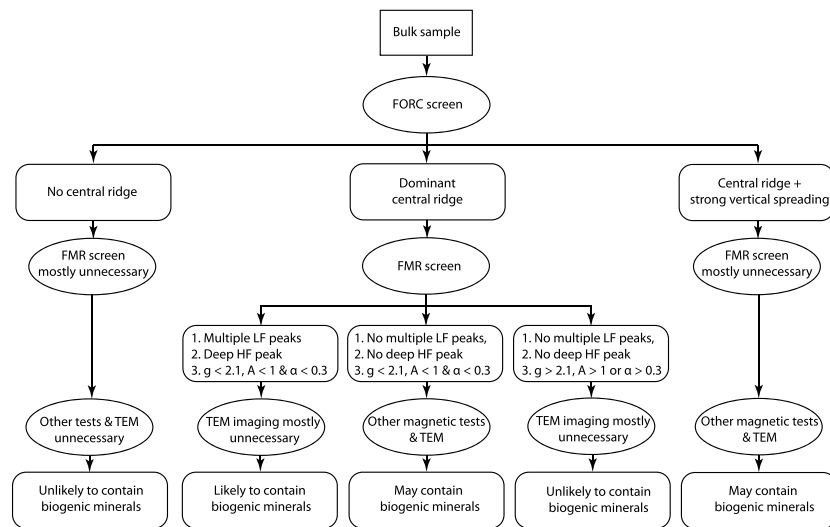
Figure 14. Proposed magnetic protocol, involving FORC diagrams, FMR spectroscopy, other magnetic methods, and TEM analysis for identifying biogenic magnetite within sediment samples. The FMR criteria for identifying biogenic magnetite chains, e.g., multiple low-field peaks, deep high-field peak, and FMR parameters with $g_{eff} < 2.1$, $A < 1$, and $\alpha < 0.3$, are from *Weiss et al.* [2004] and *Kopp et al.* [2006a, 2006b]. Sometimes FMR spectral decomposition is needed in addition to analyses of spectral shape and bulk FMR parameters.

the strength of the induced shape anisotropy from chain assembly and is potentially useful for characterizing magnetofossil preservation. In contrast, FORC diagrams are sensitive to magnetostatic interactions, but are much less sensitive to shape anisotropy compared to FMR spectroscopy. A FORC central ridge can also originate from isolated SD magnetic mineral grains. Determination of the origin of a central ridge FORC signature is often necessary.

The most distinctive advantage of FORC analysis is that it provides separate measures of coercivity and magnetostatic interaction field distributions [*Pike et al.*, 1999; *Roberts et al.*, 2000]. More importantly, the central ridge feature is fully selective of SD grains [*Egli et al.*, 2010], which makes it ideal for detecting biogenic SD minerals. Our results indicate that the biogenic FMR signature can be obscured by nonbiogenic magnetic mineral components. The origin of this biogenic signature is more likely to be evident in FORC diagrams (Figures 6 and 7), although FMR unmixing can enable recognition of biogenic signatures (Figures 4d, 5b, 6e, and 6f) [*Kopp et al.*, 2006a, 2006b; *Maloof et al.*, 2007; *Gehring et al.*, 2011]. Magnetic unmixing using FORC diagrams can also be complicated, for example, when magnetostatic interactions are present [*Muxworthy et al.*, 2005]. However, the central ridge signature is independent of such issues and unmixing is possible [*Ludwig et al.*, 2013; *Roberts et al.*, 2013; *Heslop et al.*, 2014]. Compared to FMR analysis, a noninteracting FORC signature with a 20–60 mT peak switching field probably provides a more rapid tool to detect possible biogenic magnetite in magnetically mixed samples.

Based on our analyses of diverse sediment samples, we suggest a protocol for identifying biogenic magnetite within natural samples (Figure 14). This procedure involves three main steps: (1) FORC screen → (2) FMR screen → (3) additional rock magnetic tests and TEM analysis. First, samples are subjected to FORC analysis. The next steps depend on the results from step 1.

1. If a sample does not give rise to a FORC central ridge signature, there is unlikely to be a significant amount of biogenic magnetite. No further experimental studies, including FMR and other rock magnetic analyses, are probably needed.

2. If samples pass the FORC test (i.e., there is a FORC central ridge component), but also have strong non-central ridge components, FMR analysis is probably not necessary. This is mainly because the FMR signal due to biogenic magnetite can be strongly obscured by nonbiogenic magnetic components. In this case, other rock magnetic tests for biogenic minerals and TEM imaging of magnetic extracts are needed.

3. If the FORC test is strongly positive, i.e., there is a dominant FORC central ridge component, FMR analysis is strongly recommended as a further test. If the FMR test is also positive, i.e., samples pass the FMR criteria suggested by *Weiss et al.* [2004] and *Kopp et al.* [2006a, 2006b], the tested samples probably contain significant amounts of biogenic magnetite.

Therefore, time-consuming TEM imaging and other magnetic measurements are mostly not needed. If the FMR test is negative, this probably indicates an absence of biogenic magnetite. If FMR signals contain clues of a biogenic signature (e.g., FMR parameters fall within the regions expected for intact biogenic minerals), the sample might still contain significant biogenic magnetite. In this case, additional magnetic tests and TEM imaging are needed for confirmation. In some cases, FMR tests for biogenic magnetite based on spectral shape and bulk FMR parameters can be ambiguous. FMR simulation and spectral decomposition can then be employed to improve the robustness of evidence for biogenic magnetite. This rock magnetic protocol will assist future studies in which FORC and FMR analyses are employed to detect biogenic magnetite in sediments.

6. Conclusions

We have tested the usefulness of FMR and FORC analyses for detecting and characterizing biogenic magnetite within diverse sediment samples. Our analyses enable documentation of biogenic and nonbiogenic magnetic signatures. FMR spectroscopy is sensitive to biogenic mineral chain structures, which are much less obvious in the FORC central ridge feature. A positive FMR test for biogenic magnetite provides a strong diagnostic indicator of the presence of intact biogenic magnetite chains. However, inorganic magnetic mineral assemblages, such as some TC tuff samples, can have FMR characteristics similar to those of intact biogenic magnetite. FMR spectroscopy alone, therefore, does not always provide unique identification of biogenic magnetic minerals in natural samples, although the FMR method provides a strong test. Biogenic FMR signatures can be largely obscured in FMR spectra for samples containing mixed magnetic mineral assemblages. For example, a sample containing intact biogenic magnetite, collapsed magnetosome chains, and detrital magnetic minerals does not provide a clear FMR signature for biogenic magnetic minerals. Using a new FMR decomposition technique, FMR signatures for biogenic magnetite can be recognized and characterized in mixed samples. Even for magnetofossil-dominated pelagic marine carbonates, intact magnetosome chains alone cannot explain the measured FMR spectra, which is in contrast to cultured MTB samples that contain mostly intact biogenic magnetite chains. This probably indicates significant magnetosome chain alteration within natural samples. FMR spectroscopy, therefore, potentially provides a sensitive tool to characterize magnetofossil chain configuration. FORC diagrams are superior for directly separating biogenic from nonbiogenic components in mixed samples. A central ridge FORC signature with a peak switching field between 20 and 60 mT is useful for rapidly recognizing the possible presence of biogenic magnetite. Although FMR and FORC measurements alone do not provide unique signatures for biogenic magnetite, combining these two analyses should enable discrimination in many types of samples. We suggest a three-step magnetic protocol for identifying biogenic magnetite: FORC screen → FMR screen → other magnetic tests and TEM analysis. This approach should improve the efficiency and robustness of biogenic magnetite identification, which will aid its detection in a wide range of natural environments.

References

Abrajevitch, A., and K. Kodama (2009), Biochemical vs. detrital mechanism of remanence acquisition in marine carbonates: A lesson from the K-T boundary interval, *Earth Planet. Sci. Lett.*, *286*, 269–277.

Bazylinski, D. A., and R. B. Frankel (2004), Magnetosome formation in prokaryotes, *Nature Rev. Microbiol.*, *2*, 217–230.

Bickford, L. R., Jr. (1950), Ferromagnetic resonance absorption in magnetite single crystals, *Phys. Rev.*, *78*, 449–457.

Bohaty, S. M., J. C. Zachos, F. Florindo, and M. L. Delaney (2009), Coupled greenhouse warming and deep-sea acidification in the middle Eocene, *Paleoceanography*, *24*, PA2207, doi:10.1029/2008PA001676.

Carter-Stiglitz, B., B. Moskowitz and M. Jackson (2004), More on the low-temperature magnetism of stable single domain magnetite: Reversibility and non-stoichiometry, *Geophys. Res. Lett.*, *31*, L06606, doi:10.1029/2003GL019155.

Chang, L., A. P. Roberts, W. Williams, J. D. Fitz Gerald, J. C. Larrasoaña, L. Jovane, and A. R. Muxworthy (2012a), Giant magnetofossils and hyperthermal events, *Earth Planet. Sci. Lett.*, *351–352*, 258–269, doi:10.1016/j.epsl.2012.07.031.

Chang, L., M. Winklhofer, A. P. Roberts, M. J. Dekkers, C.-S. Horng, L. Hu, and Q. W. Chen (2012b), Ferromagnetic resonance characterization of greigite (Fe_3S_4), monoclinic pyrrhotite (Fe_7S_8) and non-interacting titanomagnetite ($Fe_{3-x}Ti_xO_4$), *Geochem. Geophys. Geosyst.*, *13*, Q05Z41, doi:10.1029/2012GC004063.

Chang, L., M. Winklhofer, A. P. Roberts, D. Heslop, F. Florindo, M. J. Dekkers, W. Krijgsman, K. Kodama, and Y. Yamamoto (2013), Low-temperature magnetic properties of pelagic carbonates: Oxidation of biogenic magnetite and identification of magnetosome chains, *J. Geophys. Res. Solid Earth*, 118, 6049–6065, doi:10.1002/2013JB010381.

Charilaou, M., M. Winklhofer, and A. U. Gehring (2011a), Simulation of ferromagnetic resonance spectra of linear chains of magnetite nanocrystals, *J. Appl. Phys.*, 109, 093903, doi:10.1063/1.3581103.

Charilaou, M., K. K. Sahu, D. Faivre, A. Fischer, I. García-Rubio, and A. U. Gehring (2011b), Evolution of magnetic anisotropy and thermal stability during nanocrystal-chain growth, *Appl. Phys. Lett.*, 99, 182504, doi:10.1063/1.3658387.

Chen, A. P., R. Egli, and B. M. Moskowitz (2007), First-order reversal curve (FORC) diagrams of natural and cultured biogenic magnetic particles, *J. Geophys. Res.*, 112, B08S90, doi:10.1029/2006JB004575.

de Leeuw, A., O. Mandic, H. de Bruijn, Z. Marković, J. Reumer, W. Wessels, E. Šišić, and W. Krijgsman (2011), Magnetostratigraphy and small mammals of the Late Oligocene Banovići basin in NE Bosnia and Herzegovina, *Palaeogeogr. Palaeoclimatol. Palaeoecol.*, 310, 400–412.

de Leeuw, A., O. Mandic, W. Krijgsman, K. F. Kuiper, and H. Hrvatovic (2012), Paleomagnetic and geochronologic constraints on the geodynamic evolution of the Central Dinarides, *Tectonophysics*, 530–531, 286–298.

Dunin-Borkowski, R. E., M. R. McCartney, R. B. Frankel, D. A. Bazylinski, M. Posfai, and P. R. Buseck (1998), Magnetic microstructure of magnetotactic bacteria by electron holography, *Science*, 282, 1868–1870.

Egli, R. (2004a), Characterization of individual rock magnetic components by analysis of remanence curves: 1. Unmixing natural sediments, *Stud. Geophys. Geod.*, 48, 391–446, doi:10.1023/B:SGEG.0000020839.45304.6d.

Egli, R. (2004b), Characterization of individual rock magnetic components by analysis of remanence curves. 2. Fundamental properties of coercivity distributions, *Phys. Chem. Earth*, 29, 851–867.

Egli, R. (2013), VARIFORC: An optimized protocol for calculating non-regular first-order reversal curve (FORC) diagrams, *Global Planet. Change*, 110, 302–320.

Egli, R., A. P. Chen, M. Winklhofer, K. P. Kodama, and C.-S. Horng (2010), Detection of noninteracting single domain particles using first-order reversal curve diagrams, *Geochem. Geophys. Geosyst.*, 11, Q01Z11, doi:10.1029/2009GC002916.

Faivre, D., and D. Schüler (2008), Magnetotactic bacteria and magnetosomes, *Chem. Rev.*, 108, 4875–4898, doi:10.1021/cr078258w.

Fischer, H., J. Luster, and A. U. Gehring (2007), EPR evidence for maghemitization of magnetite in a tropical soil, *Geophys. J. Int.*, 169, 909–916.

Fischer, H., G. Mastrogiacomo, J. F. Löffler, R. J. Warthmann, P. G. Weidler, and A. U. Gehring (2008), Ferromagnetic resonance and magnetic characteristics of intact magnetosome chains in *Magnetospirillum gryphiswaldense*, *Earth Planet. Sci. Lett.*, 270, 200–208, doi:10.1016/j.epsl.2008.03.022.

Florindo, F., and A. P. Roberts (2005), Eocene-Oligocene magnetobiostratigraphy of ODP sites 689 and 690, Maud Rise, Weddell Sea, Antarctica, *Geol. Soc. Am. Bull.*, 117, 46–66, doi:10.1130/B25541.1.

Gehring, A. U., J. Kind, M. Charilaou, and I. García-Rubio (2011), The detection of magnetotactic bacteria and magnetofossils by means of magnetic anisotropy, *Earth Planet. Sci. Lett.*, 309, 113–117, doi:10.1016/j.epsl.2011.06.024.

Gehring, A. U., M. Charilaou, and I. García-Rubio (2012), Oxidized magnetosomes in magnetotactic bacteria, *J. Magn. Magn. Mater.*, 324, 1281–1284.

Gehring, A. U., J. Kind, M. Charilaou, and I. García-Rubio (2013), S-band ferromagnetic resonance spectroscopy and the detection of magnetofossils, *J. R. Soc. Interface*, 10, 20120790, doi:10.1098/rsif.2012.0790.

Geiss, C. E., R. Egli, and W. Zanner (2008), Direct estimates of pedogenic magnetite as a tool to reconstruct past climates from buried soils, *J. Geophys. Res.*, 113, B11102, doi:10.1029/2008JB005669.

Heslop, D., and A. P. Roberts (2012), Estimation of significance levels and confidence intervals for first-order reversal curve distributions, *Geochem. Geophys. Geosyst.*, 13, Q12Z40, doi:10.1029/2012GC004115.

Heslop, D., A. P. Roberts, L. Chang, M. Davies, A. Abrajevitch, and P. De Deckker (2013), Quantifying magnetite magnetofossil contributions to sedimentary magnetizations, *Earth Planet. Sci. Lett.*, 382, 58–65.

Heslop, D., A. P. Roberts, and L. Chang (2014), Recognition of biogenic magnetite components from first-order reversal curve signatures, *Geochem. Geophys. Geosyst.*, 15, 255–283, doi:10.1002/2014GC005301.

Hesse, P. P. (1994), Evidence for bacterial palaeoecological origin of mineral magnetic cycles in oxic and sub-oxic Tasman Sea sediments, *Mar. Geol.*, 117, 1–17.

Hounslow, M. W., and B. A. Maher (1996), Quantitative extraction and analysis of carriers of magnetization in sediments, *Geophys. J. Int.*, 124, 57–74.

Housen, B. A., and B. M. Moskowitz (2006), Depth distribution of magnetofossils in near-surface sediments from the Blake/Bahama Outer Ridge, western North Atlantic Ocean, determined by low-temperature magnetism, *J. Geophys. Res.*, 111, G01005, doi:10.1029/2005JG000068.

Jackson, M., B. Carter-Stiglitz, R. Egli, and P. Solheid (2006), Characterizing the superparamagnetic grain distribution $f(V, H_k)$ by thermal fluctuation tomography, *J. Geophys. Res.*, 111, B12S07, doi:10.1029/2006JB004514.

Kind, J., A. U. Gehring, M. Winklhofer, and A. M. Hirt (2011), Combined use of magnetometry and spectroscopy for identifying magnetofossils in sediments, *Geochem. Geophys. Geosyst.*, 12, Q08008, doi:10.1029/2011GC003633.

Kind, J., U. J. V. Raden, I. García-Rubio, and A. U. Gehring (2012), Rock magnetic techniques complemented by ferromagnetic resonance spectroscopy to analyse a sediment record, *Geophys. J. Int.*, 191, 51–63.

Kirschvink, J. L., and S.-B. R. Chang (1984), Ultrafine-grained magnetite in deep-sea sediments: Possible bacterial magnetofossils, *Geology*, 12, 559–562.

Kodama, K. P., R. E. Moeller, D. A. Bazylinski, R. E. Kopp, and A. P. Chen (2013), The mineral magnetic record of magnetofossils in recent lake sediments of Lake Ely, PA, *Global Planet. Change*, 110, 350–363.

Kopp, R. E., and J. L. Kirschvink (2008), The identification and biogeochemical interpretation of fossil magnetotactic bacteria, *Earth Sci. Rev.*, 86, 42–61.

Kopp, R. E., C. Z. Nash, A. Kobayashi, B. P. Weiss, D. A. Bazylinski, and J. L. Kirschvink (2006a), Ferromagnetic resonance spectroscopy for assessment of magnetic anisotropy and magnetostatic interactions: A case study of mutant magnetotactic bacteria, *J. Geophys. Res.*, 111, B12S25, doi:10.1029/2006JB004529.

Kopp, R. E., B. P. Weiss, A. C. Maloof, H. Vali, C. Z. Nash, and J. L. Kirschvink (2006b), Chains, clumps, and strings: Magnetofossil taphonomy with ferromagnetic resonance spectroscopy, *Earth Planet. Sci. Lett.*, 247, 10–25.

Kopp, R. E., T. D. Raub, D. Schumann, H. Vali, A. V. Smirnov, and J. L. Kirschvink (2007), Magnetofossil spike during the Paleocene-Eocene thermal maximum: Ferromagnetic resonance, rock magnetic, and electron microscopy evidence from Ancora New Jersey, United States, *Paleoceanography*, 22, PA4103, doi:10.1029/2007PA001473.

Kopp, R. E., D. Schumann, T. D. Raub, D. S. Powars, L. V. Godfrey, N. L. Swanson-Hysell, A. C. Maloof, and H. Vali (2009), An Appalachian Amazon? Magnetofossil evidence for the development of a tropical river-like system in the mid-Atlantic United States during the Paleocene-Eocene Thermal Maximum, *Paleoceanography*, 24, PA4211, doi:10.1029/2009PA001783.

Kruiver, P. P., and H. F. Passier (2001), Coercivity analysis of magnetic phases in sapropel S1 related to variations in redox conditions, including an investigation of the S ratio, *Geochem. Geophys. Geosyst.*, 2, 1063, doi:10.1029/2001GC000181.

Larrasoaña, J. C., A. P. Roberts, L. Chang, S. A. Schellenberg, J. D. Fitz Gerald, R. D. Norris, and J. C. Zachos (2012), Magnetotactic bacterial response to Antarctic dust supply during the Palaeocene-Eocene thermal maximum, *Earth Planet. Sci. Lett.*, 333–334, 122–133, doi:10.1016/j.epsl.2012.04.003.

Lean, C. M. B., and I. N. McCave (1998), Glacial to interglacial mineral magnetic and palaeoceanographic changes at Chatham Rise, SW Pacific Ocean, *Earth Planet. Sci. Lett.*, 163, 247–260.

Li, J., Y. Pan, G. Chen, Q. Liu, L. Tian, and W. Lin (2009), Magnetite magnetosome and fragmental chain formation of *Magnetospirillum magneticum* AMB-1: Transmission electron microscopy and magnetic observations, *Geophys. J. Int.*, 177, 33–42, doi:10.1111/j.1365-246X.2009.04043.x.

Li, J., et al. (2010), Biomineralization, crystallography and magnetic properties of bullet-shaped magnetite magnetosomes in giant rod magnetotactic bacteria, *Earth Planet. Sci. Lett.*, 293, 368–376.

Li, J., W. Wu, Q. Liu, and Y. Pan (2012), Magnetic anisotropy, magnetostatic interactions and identification of magnetofossils, *Geochem. Geophys. Geosyst.*, 13, Q10Z51, doi:10.1029/2012GC004384.

Lin, W., and Y. Pan (2009), Uncultivated magnetotactic cocci from Yuandadu Park in Beijing, China, *Appl. Environ. Microbiol.*, 75, 4046–4052.

Ludwig, P., R. Egli, S. Bishop, V. Chernenko, T. Frederichs, G. Rugel, and S. Merchel (2013), Characterization of primary and secondary magnetite in marine sediment by combining chemical and magnetic unmixing techniques, *Global Planet. Change*, 110, 321–339.

Maloof, A. C., R. E. Kopp, J. P. Grotzinger, D. A. Fike, T. Bosak, H. Vali, P. M. Poussart, B. P. Weiss, and J. L. Kirschvink (2007), Sedimentary iron cycling and the origin and preservation of magnetization in platform carbonate muds, Andros Island, Bahamas, *Earth Planet. Sci. Lett.*, 259, 581–598, doi:10.1016/j.epsl.2007.05.021.

Moskowitz, B. M., R. B. Frankel, and D. A. Bazylinski (1993), Rock magnetic criteria for the detection of biogenic magnetite, *Earth Planet. Sci. Lett.*, 120, 283–300, doi:10.1016/0012-821X(93)90245-5.

Moskowitz, B. M., D. A. Bazylinski, R. Egli, R. B. Frankel, and K. J. Edwards (2008), Magnetic properties of marine magnetotactic bacteria in a seasonally stratified coastal pond (Salt Pond, MA, USA), *Geophys. J. Int.*, 174, 75–92, doi:10.1111/j.1365-246X.2008.03789.x.

Muxworthy, A. R., and D. J. Dunlop (2002), First-order reversal curve (FORC) diagrams for pseudo-single-domain magnetites at high temperature, *Earth Planet. Sci. Lett.*, 203, 369–382.

Muxworthy, A. R., J. G. King, and D. Heslop (2005), Assessing the ability of first-order reversal curve (FORC) diagrams to unravel complex magnetic signals, *J. Geophys. Res.*, 110, B01105, doi:10.1029/2004JB003195.

Oba, T., T. Irino, M. Yamamoto, M. Murayama, A. Takamura, and K. Aoki (2006), Paleoceanographic change off central Japan since the last 144,000 years based on high-resolution oxygen and carbon isotope records, *Global Planet. Change*, 53, 5–20.

Pan, Y., N. Petersen, M. Winklhofer, A. F. Davila, Q. Liu, T. Frederichs, M. Hanzlik, and R. Zhu (2005), Rock magnetic properties of uncultured magnetotactic bacteria, *Earth Planet. Sci. Lett.*, 237, 311–325, doi:10.1016/j.epsl.2005.06.029.

Passier, H. F., and M. J. Dekkers (2002), Iron oxide formation in the active oxidation front above sapropel S1 in the eastern Mediterranean Sea as derived from low-temperature magnetism, *Geophys. J. Int.*, 150, 230–240, doi:10.1046/j.1365-246X.2002.01704.x.

Peck, J. A., and J. W. King (1996), Magnetofossils in the sediment of Lake Baikal, Siberia, *Earth Planet. Sci. Lett.*, 140, 159–172, doi:10.1016/0012-821X(96)00027-1.

Penninga, I., H. de Waard, B. M. Moskowitz, D. A. Bazylinksi, and R. B. Frankel (1995), Remanence measurements on individual magnetotactic bacteria using a pulsed magnetic field, *J. Magn. Magn. Mater.*, 149, 279–286.

Petersen, N., T. von Dobeneck, and H. Vali (1986), Fossil bacterial magnetite in deep-sea sediments from the South Atlantic Ocean, *Nature*, 320, 611–614.

Pike, C. R., A. P. Roberts, and K. L. Verosub (1999), Characterizing interactions in fine magnetic particle systems using first order reversal curves, *J. Appl. Phys.*, 85, 6660–6667, doi:10.1063/1.370176.

Pike, C. R., A. P. Roberts, and K. L. Verosub (2001a), First-order reversal curve diagrams and thermal relaxation effects in magnetic particles, *Geophys. J. Int.*, 145, 721–730.

Pike, C. R., A. P. Roberts, M. J. Dekkers, and K. L. Verosub (2001b), An investigation of multi-domain hysteresis mechanisms using FORC diagrams, *Phys. Earth Planet. Inter.*, 126, 11–25.

Reinholdsson, M., I. Snowball, L. Zillén, C. Lenz, and D. J. Conley (2013), Magnetic enhancement of Baltic Sea sapropels by greigite magnetofossils, *Earth Planet. Sci. Lett.*, 366, 137–150.

Roberts, A. P., Y. L. Cui, and K. L. Verosub (1995), Wasp-waisted hysteresis loops: Mineral magnetic characteristics and discrimination of components in mixed magnetic systems, *J. Geophys. Res.*, 100, 17,909–17,924, doi:10.1029/95JB00672.

Roberts, A. P., C. R. Pike, and K. L. Verosub (2000), First-order reversal curve diagrams: A new tool for characterizing the magnetic properties of natural samples, *J. Geophys. Res.*, 105, 28,461–28,475, doi:10.1029/2000JB900326.

Roberts, A. P., Q. Liu, C. J. Rowan, L. Chang, C. Carvallo, J. Torrent, and C. S. Horng (2006), Characterization of hematite (α-Fe2O3), goethite (α-FeOOH), greigite (Fe$_3$S$_4$), and pyrrhotite (Fe$_7$S$_8$) using first-order reversal curve diagrams, *J. Geophys. Res.*, 111, B12S35, doi:10.1029/2006JB004715.

Roberts, A. P., F. Florindo, G. Villa, L. Chang, L. Jovane, S. M. Bohaty, J. C. Larrasoaña, D. Heslop, and J. D. Fitz Gerald (2011), Magnetotactic bacterial abundance in pelagic marine environments is limited by organic carbon flux and availability of dissolved iron, *Earth Planet. Sci. Lett.*, 310, 441–452, doi:10.1016/j.epsl.2011.08.011.

Roberts, A. P., L. Chang, D. Heslop, F. Florindo, and J. C. Larrasoaña (2012), Searching for single domain magnetite in the "pseudo-single-domain" sedimentary haystack: Implications of biogenic magnetite preservation for sediment magnetism and relative paleointensity determinations, *J. Geophys. Res.*, 117, B08104, doi:10.1029/2012JB009412.

Roberts, A. P., F. Florindo, L. Chang, D. Heslop, L. Jovane, and J. C. Larrasoaña (2013), Magnetic properties of pelagic marine carbonates, *Earth Sci. Rev.*, 127, 111–139.

Robertson, D. J., and D. E. France (1994), Discrimination of remanence-carrying minerals in mixtures, using isothermal remanent magnetisation acquisition curves, *Phys. Earth Planet. Inter.*, 82, 223–234.

Rosenbaum, J. G. (1993), Magnetic grain-size variations through an ash flow sheet: Influence on magnetic properties and implications for cooling history, *J. Geophys. Res.*, 98, 11,715–11,727, doi:10.1029/93JB00355.

Rowan, C. J., A. P. Roberts, and T. Broadbent (2009), Reductive diagenesis, magnetite dissolution, greigite growth and paleomagnetic smoothing in marine sediments: A new view, *Earth Planet. Sci. Lett.*, 277, 223–235.

Schlinger, C. M., D. R. Veblen, and J. G. Rosenbaum (1991), Magnetism and magnetic mineralogy of ash flow tuffs from Yucca Mountain, Nevada, *J. Geophys. Res.*, 96, 6035–6052, doi:10.1029/90JB02653.

Smirnov, A. V., and J. A. Tarduno (2000), Low-temperature magnetic properties of pelagic sediments (Ocean Drilling Program Site 805C): Tracers of maghemitization and magnetic mineral reduction, *J. Geophys. Res.*, *105*, 16,457–16,471, doi:10.1029/2000JB900140.

Stoltz, J. F., S. B. R. Chang, and J. L. Kirschvink (1986), Magnetotactic bacteria and single-domain magnetite in hemipelagic sediments, *Nature*, *321*, 849–851.

Tauxe, L., T. A. T. Mullender, and T. Pick (1996), Pot-bellies wasp-waists and superparamagnetism in magnetic hysteresis, *J. Geophys. Res.*, *101*, 571–583.

Till, J. L., M. J. Jackson, J. G. Rosenbaum, and P. Solheid (2011), Magnetic properties in an ash flow tuff with continuous grain size variation: A natural reference for magnetic particle granulometry, *Geochem. Geophys. Geosyst.*, *12*, Q07Z26, doi:10.1029/2011GC003648.

Vali, H., O. Förster, G. Amarantidis, and N. Petersen (1987), Magnetotactic bacteria and their magnetofossils in sediments, *Earth Planet. Sci. Lett.*, *86*, 389–400, doi:10.1016/0012-821X(87)90235-4.

Valstyn, E. P., J. P. Hanton, and A. H. Morrish (1962), Ferromagnetic resonance of single-domain particles, *Phys. Rev.*, *128*, 2078–2087.

van Oorschot, I. H. M., M. J. Dekkers, and P. Havlicek (2002), Selective dissolution of magnetic iron oxides with the acid-ammonium-oxalate/ferrous-iron extraction technique—II. Natural loess and palaeosol samples, *Geophys. J. Int.*, *149*, 106–117.

Vasiliev, I., C. Franke, J. D. Meeldijk, M. J. Dekkers, C. G. Langereis, and W. Krijgsman (2008), Putative greigite magnetofossils from the Pliocene Epoch, *Nat. Geosci.*, *1*, 782–786.

Weiss, B. P., S. S. Kim, J. L. Kirschvink, R. E. Kopp, M. Sankaran, A. Kobayashi, and A. Komeili (2004), Ferromagnetic resonance and low temperature magnetic tests for biogenic magnetite, *Earth Planet. Sci. Lett.*, *224*, 73–89.

Winklhofer, M., L. Chang, and S. H. K. Eder (2014), On the magnetocrystalline anisotropy of greigite (Fe_3S_4), *Geochem. Geophys. Geosyst.*, *15*, 1558–1579, doi:10.1002/2013GC005121.

Worm, H.-U., and M. Jackson (1999), The superparamagnetism of Yucca Mountain Tuff, *J. Geophys. Res.*, *104*, 25,415–25,425, doi:10.1029/1999JB900285.

Yamazaki, T., and M. Ikehara (2012), Origin of magnetic mineral concentration variation in the Southern Ocean, *Paleoceanography*, *27*, PA2206, doi:10.1029/2011PA002271.

Zhao, X., and A. P. Roberts (2010), How does Chinese loess become magnetized?, *Earth Planet. Sci. Lett.*, *292*, 112–122.